Directed Assembly of Block Copolymers by Sparsely Patterned Substrates

5 AUTHORS, INCLUDING:

Yury Anatolievich Kriksin
Russian Academy of Sciences
13 PUBLICATIONS **155** CITATIONS

SEE PROFILE

Pavel G. Khalatur
Universität Ulm
235 PUBLICATIONS **2,487** CITATIONS

SEE PROFILE

Irina V. Neratova
9 PUBLICATIONS **58** CITATIONS

SEE PROFILE

Larisa Tsarkova
RWTH Aachen University
56 PUBLICATIONS **682** CITATIONS

SEE PROFILE

Directed Assembly of Block Copolymers by Sparsely Patterned Substrates

Yury A. Kriksin,[†] Pavel G. Khalatur,*[,‡,§] Irina V. Neratova,[‡,||] Alexei R. Khokhlov,[‡,⊥] and Larisa A. Tsarkova*[,#]

[†]Institute for Mathematical Modeling, Russian Academy of Science, Moscow 125047, Russia

[‡]Department of Polymer Science, University of Ulm, Ulm-89069, Germany

[§]Institute of Organoelement Compounds, Russian Academy of Science, Moscow 119991, Russia

[||]Department of Physical Chemistry, Tver State University, Tver, 170002, Russia

[⊥]Physics Department, Moscow State University, Moscow 119899, Russia

[#]DWI an der RWTH Aachen e.V., 52064 Aachen, Germany

ABSTRACT: Self-consistent field theory and dissipative particle dynamics simulations are used to demonstrate the controlled positioning and alignment of cylindrical domains by chemical surface patterns in an asymmetric slit. Self-assembly of the copolymer melt is simulated near dense and sparse surface patterns, both with one and two characteristic length scales. In particular, we compare the effect of a hexagonal pattern, sparse rectangular pattern, and triangle pattern. The parallel alignment of microdomains between preferentially attractive homogeneous

surfaces is shown to transform into the stable perpendicular hexagonal phase in the case of the substrate patterns, which commensurate with the hexagonal morphology in the bulk. For the sparse rectangular pattern, when two different length scales of interactions are involved, and for the sparse hexagonal pattern, we observe that the self-assembly of diblocks multiplies the density of the surface patterns by a factor of 2 and 4, respectively. A 2-fold resolution enhancement was found for sparse triangle pattern with two characteristic length scales. The analysis of the circularly averaged structure factor allowed us to distinguish the structure orientation in a film. Additional peak in the region of small lateral wave numbers is attributed to undulational deformations of cylinder domains under preferable film boundaries. This theoretical work serves to rationalize modern nanolithographic fabrication of high-spatial-frequency arrays using lower-spatial-frequency templates.
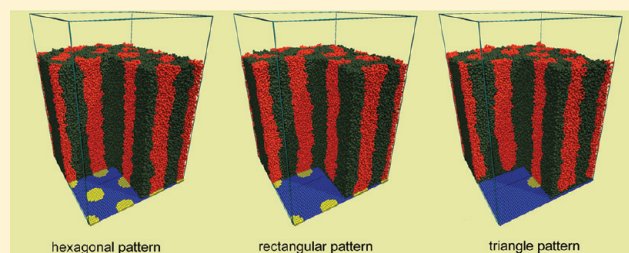
1. INTRODUCTION

Self-assembly of block copolymers (BCPs) is a simple and low-cost route to engineer highly organized functional nanometer-scale patterns.[1−4] Depending on the internal parameters such as molecular architecture, chemical composition, chain flexibility, and mutual interaction of the chemically distinct segments and on the external parameters such as the degree of confinement, the surface/interface energies, and the presence of the external fields, BCPs in thin films can be tailored to spontaneously order via a thermally driven phase separation and surface fields effects to form a number of equilibrium morphologies with tunable nanoscale dimensions.[3−12] Intensive research on the phase behavior of BCPs in thin films convincingly demonstrated the feasibility of these systems for designing a new generation of electronic devices and templates for the fabrication of nanowires, quantum dots, or catalyst arrays for carbon nanotube growth.[13−23] However, the utilization of this potential depends to a large extent on our ability to control the ordering and orientation of the nanoscopic domains (known as registration). For instance, morphology with perpendicular cylindrical domains is desirable for most of the practical applications, whereas cylinders parallel to the surface are not particularly useful.[23−25]

Modification of the interfacial interactions at the film substrate (surface field effect) is a thermodynamics-based approach which has proved to be an effective and robust toward experimental perturbation methods to manipulate the microphase separation and structure orientation both at the polymer/substrate interface and in the interior of the films. On the basis of the interplay of the interfacial energies, directed self-assembly (DSA) is the most promising approach to precisely register microphase separated structures by using artificial topographical or chemically prepatterned templates.[26−32] In the chemical epitaxy method, which is similar to conventional epitaxy in a crystalline film, the self-assembly of BCPs is guided by a surface energy pattern on the substrate. This pattern typically comprises areas with different surface energies so that chemically distinct copolymer blocks wet preferentially different parts of the surface.[28] The affinity between the nanometer-scale chemical pattern and at least one of the types of BCP microdomains can be used to create high-

quality BCP arrays with well-registered domains which directly mirror the underlying chemical pattern.[33,34]

The major restriction of both graphoepitaxy and chemical epitaxy methods is related to the lithographic limitations in masks fabrication.[35] In this regard, significant enhancements in lithographic capabilities can be expected from a recently developed approach that combines the advantages of directed BCP assembly with those provided by the conventional lithographic techniques.[36−44] This approach can provide enhanced patterns over those written into a substrate. The main idea here is to multiply a relatively sparse surface pattern using BCP self-assembly, thereby making it possible to double, triple, quadruple, and so on the frequencies of the pattern with no loss in orientational control or increase in defects. As a result, this approach offers high potential to increase the feature density and to lower the costs of creating regular nanopatterns over large areas. In particular, using sparse chemical patterns and compositionally symmetric BCPs, Cheng et al. reported defect-free alignment of lamellae and demonstrated that the self-assembly process can interpolate points in between the lithography-generated pattern.[36] Ruiz et al.[37] and Bita et al.[38] also reported density multiplication and rectification effects of chemical and topographic patterns for cylindrical and spherical microdomains, respectively. Importantly, a key feature of chemical epitaxy is that the surface patterns can deviate as much 20 or 30% different from the block copolymer dimensions.[37] Tada at al. addressed the formation of perpendicular cylindrical domains and showed that a 9-fold feature density multiplication can be attained with a combination of lithography and self-assembled patterning.[39,40] Xiao et al. used e-beam lithography to create nanodots on the substrate preferential for the minority component in a sphere-forming diblock and demonstrated frequency multiplication by a factor of 9 with translational order extending over the entire patterned area.[41] These results have profound implications for advancing the performance and capabilities of lithographic materials and processes beyond current limits. It is expected that with this combined technique, the fabrication of defect-free arrays of BCP domains is possible at densities up to 10 Tdot/in².[45]

In theoretical work, primarily the Monte Carlo method has been employed to study the concept of density multiplication in BCP lithography.[37,46−51] The authors simulated both symmetric[37,46−48] and asymmetric[37,49−51] block copolymers on patterned surfaces, using the Monte Carlo method and the so-called theoretically informed coarse grain (TICG) model.[52−54] For cylinder-forming diblock copolymers and their ternary blends with homopolymers, it was shown that self-assembly on hexagonally arranged surface patterns can result in a 4-fold increase in feature density.[37,49−51] A self-consistent field theory study on DSA of copolymers by patterned substrates has been so far a challenge.[55]

In this paper, using the combination of self-consistent field theory (SCFT) and dissipative particle dynamics (DPD), we investigate pattern multiplication by cylinder-forming copolymers that self-assemble near surface patterns with one and with two characteristic length scales. In particular, we compare the effect of (i) the hexagonal pattern, (ii) the sparse rectangular pattern, and (iii) the triangular pattern. Note that the generation of rectangular (square) nanopatterns has recently been described by Tang et al.[56] Additionally, we analyze the circularly averaged structure factor, which is typically obtained from scattering experiments.[57] In experiments, such analysis is a widespread technique to determine the density profile perpendicular to the film surface and the undulational deformations of cylinder domains.

2. MODEL AND SIMULATION METHODS

2.1. Self-Consistent Field Theory.
We consider an incompressible melt of AB diblock copolymer in a thin-film geometry of thickness h. n chains each of length N are confined in a slit which is defined by two surfaces that are located at $z = 0$ and $z = h$. The two surfaces in the z direction are hard walls, that is, no monomers can penetrate from the system through the surfaces. The periodic boundary conditions are imposed on the x and y directions. Each copolymer contains fN A-type segments joined to $(1-f)N$ B-type segments $(0 < f < 1/2)$. All segments have the same statistical length σ and volume. The Flory−Huggins segmental interaction parameter χ controls the incompatibility of the A-type and B-type segments. Since the polymer self-consistent-field theory has been well developed, we only provide a brief summary of the SCFT calculations here; readers are referred to, e.g., ref 6 for detailed derivation and explanation of this theory.

The free energy of the system is given by

$$F[\psi_A, \psi_B]/nk_BT = V^{-1}\int d^3\mathbf{r}\,[-f\psi_A(\mathbf{r}) - (1-f)\psi_B(\mathbf{r}) + (\psi_A(\mathbf{r}) - \psi_B(\mathbf{r}))^2/(4\chi N)] - \ln Q[\psi_A, \psi_B] \quad (1)$$

where V is the system volume and $Q[\psi_A, \psi_B]$ is the single-chain partition function to be defined as

$$Q[\psi_A, \psi_B] = V^{-1}\int d^3\mathbf{r}\, q(\mathbf{r}, 1; [\psi_A, \psi_B]) \quad (2)$$

The end-to-end segment distribution function $q(\mathbf{r},1;[\psi_A,\psi_B])$ satisfies the modified diffusion equation[6]

$$\frac{\partial}{\partial s}q(\mathbf{r},s) = \nabla^2 q(\mathbf{r},s) - \psi(\mathbf{r},s)q(\mathbf{r},s),$$
$$q(\mathbf{r},0) = 1, \quad 0 \leq s \leq 1 \quad (3)$$

with periodic boundary conditions in the lateral (x,y) directions and reflecting boundary conditions at the confining walls

$$\left.\frac{\partial q}{\partial z}\right|_{z=0,h} = 0 \quad (4)$$

Each polymer chain is parametrized with a variable s increasing along the chain. The values $s = 0, 1$ correspond to the chain end points while for the junction point, $s = f$. The function $\psi(\mathbf{r},s)$ in eq 3 is a sum of the self-consistent fields $\psi_\alpha(\mathbf{r})$ and the surface fields $\gamma_\alpha(\mathbf{r})$

$$\psi(\mathbf{r},s) = \psi_{\alpha(s)}(\mathbf{r}) + \gamma_{\alpha(s)}(\mathbf{r}) \quad (5)$$

where $\alpha(s) = A$ if $0 \leq s < f$ and $\alpha(s) = B$ if $f \leq s < 1$. The surface fields $\gamma_\alpha(\mathbf{r})$ describe the effect of confining walls. The total segment density vanishes on the confining walls and outside the slit. In other words, the only allowed trajectories of the polymer chains belong to the region $0 < z < h$. We assume that the top wall is homogeneous while the bottom wall can be patterned with an array of sites representing alternating A-like and B-like regions, labeled by C and D, respectively. The interaction between the polymer segments of type α ($\alpha = A, B$) and the bottom (b) and top (t) walls is characterized by the following surface field:

$$\gamma_\alpha(\mathbf{r}) = 2[\varepsilon_\alpha^{(b)}\delta(z) + \varepsilon_\alpha^{(t)}\delta(z-h)] \quad (6)$$

25186

dx.doi.org/10.1021/jp204629k | J. Phys. Chem. C 2011, 115, 25185−25200

with $\varepsilon_\alpha^{(b)} = \varepsilon_\alpha^{(D)} + (\varepsilon_\alpha^{(C)} - \varepsilon_\alpha^{(D)})\xi(x,y)$, where $\varepsilon_\alpha^{(b)}$ and $\varepsilon_\alpha^{(t)}$ describe the $\alpha-b$ and $\alpha-t$ interactions and $\varepsilon_\alpha^{(C)}$ and $\varepsilon_\alpha^{(D)}$ are the energy parameters describing the interaction between the polymer segments and the patterned surface. The periodic function $\xi(x,y)$ indicates the location of C and D regions on the substrate: $\xi(x,y) = 1$ if the point (x, y) belongs to the C site and $\xi(x,y) = 0$ otherwise. For a homogeneous surface, $\xi(x,y)$ is a constant. The prefactor 2 takes into account that the Dirac delta functions δ in eq 6 lie directly on the boundaries.[58]

The SCFT saddle-point approximation results in the following equations:

$$\varphi_A(\mathbf{r}) + \varphi_B(\mathbf{r}) - 1 = 0,$$

$$2f - 1 + \frac{1}{\chi N}[\psi_B(\mathbf{r}) - \psi_A(\mathbf{r})] + \varphi_B(\mathbf{r}) - \varphi_A(\mathbf{r}) = 0 \tag{7}$$

where the volume fractions $\varphi_A(\mathbf{r})$ and $\varphi_B(\mathbf{r})$ are defined as

$$\varphi_A(\mathbf{r}) = \frac{1}{Q[\psi_A, \psi_B]} \int_0^f ds\, q(\mathbf{r},s)\tilde{q}(\mathbf{r}, 1-s) \tag{8}$$

$$\varphi_B(\mathbf{r}) = \frac{1}{Q[\psi_A, \psi_B]} \int_f^1 ds\, q(\mathbf{r},s)\tilde{q}(\mathbf{r}, 1-s) \tag{9}$$

The function $q(\mathbf{r},s)$ is the solution of the modified diffusion eq 3 and the function $\tilde{q}(\mathbf{r},s)$ obeys the similar equation

$$\frac{\partial}{\partial s}\tilde{q}(\mathbf{r},s) = \nabla^2\tilde{q}(\mathbf{r},s) - \psi(\mathbf{r}, 1-s)\tilde{q}(\mathbf{r},s), \quad \tilde{q}(\mathbf{r}, 0) = 1 \tag{10}$$

with the same periodic boundary conditions in the lateral directions and the reflecting conditions (4). These equations identify $\varphi_A(\mathbf{r})$ and $\varphi_B(\mathbf{r})$ as the average densities of A and B chain segments at point $\mathbf{r}$ as calculated in an ensemble of macromolecules subject to the fields $\psi_A(\mathbf{r})$ and $\psi_B(\mathbf{r})$ acting on A and B segments, respectively.[6,59]

The modified diffusion eqs 3 and 10 were solved by the pseudospectral method[6,60,61] in the rectangular box of dimensions $L_x = d$, $L_y = \sqrt{3}\, d$, $L_z = h$, where d is the lateral period and h is the slit thickness. The solution of the SCFT eqs 7−9 was found by the iterative procedure described in our previous papers.[61−63]

The free energy (1) is to be minimized with respect to the lateral period d and the slit thickness h. Various runs with different initial fields were examined and the morphology with the lowest free energy was considered to be the most stable phase under given conditions. In this work, we are mainly interested in the relative stability between parallel ($C_\parallel$) and perpendicular ($C_\perp$) cylinder morphologies. The pseudospectral algorithm gives the Fourier expansion of density fields, which were used for calculating the circularly averaged structure factor $S_\parallel(q)$ (for more detail, see Appendix A).

The dimension of the parameter space in our model is sufficiently large to explore all possible cases, so we restrict ourselves to the case of $f = 0.25$ and $\chi N = 20$, when the bulk period $d_0 = 3.882R_g$. Some additional calculations were performed at $\chi N = 25$. Detcheverry et al.[49] used the same value of χN in their TICG simulation. All lengths are measured in the units of the radius of gyration, $R_g = \sigma(N/6)^{1/2}$. The fields $\psi_\alpha(\mathbf{r})$ and $\gamma_\alpha(\mathbf{r})$ as well as the energy parameters are measured in the k_BT units.

2.2. Dissipative Particle Dynamics. Because SCFT is a mean-field theory, it neglects fluctuations around the most probable configuration and actually the results that it predicts can be inaccurate in the weak segregation limit (apart from the un-physical limit of infinitely long chains). Also, the interfaces between microdomains in the SCFT calculations are ideally flat and there is no broadening by polymer density fluctuations of the local position of the interfaces.[64,65] To overcome these obstacles, complementary to our SCFT calculations, we employ continuous DPD simulations which allow us to take explicitly into account thermal fluctuations.

It should also be kept in mind that experimentally realized thin-film BCP systems normally have two different kinds of surfaces, one being a hard wall (substrate/polymer interface) and the opposite one being a free surface. Therefore, in our DPD simulations, the top surface of a film is modeled as a gas/polymer interface or "free" surface. We expect that under these conditions, the BCP film can take its natural thickness, because the possible frustrated states due to the incompatibility between film thickness and bulk period can be eliminated by deforming the shape of the present gas/polymer interface.

The DPD is a particle-based coarse-grained simulation technique in which every particle represents a collection of atoms, just like the beads in a bead−spring model of a polymer. The technical details of DPD have already been discussed intensively.[66−68] Thus, we do not repeat the discussion here, but mainly outline the governing parameters. In what follows, we use reduced units for all variables: energy unit is such that $k_BT = 1$, the bead size σ and bead mass m is taken to be unity.

In our DPD simulations, a thin film of an AB copolymer is placed in a rectangular periodic box on a solid substrate. The confining walls are located at $z = 0$ and $z = h$. The box dimensions are $L_x = L_y$ and L_z. The volume above the film is assumed to be filled with "gas" (or "solvent" particles) and the boundary between the gas phase and the polymer film corresponds to a free surface that is expected to show shape fluctuations. The effect of the free surface can be taken into account by explicitly considering the gas as a single-site component in the standard DPD calculation for polymer solutions. Therefore, the gas particle (G) is assumed to have the same size as the polymer bead, and its interaction with the polymer is specified by the DPD parameters a_{AG} and a_{BG}, which are taken to be large since polymers cannot diffuse into the gas. The initial state of the system consists of two phases: one is the gas phase in the upper region of the simulation box, and the other is the polymer film close to a solid substrate covered with alternating wettable domains of the C and D type, which exhibit different chemical affinities toward A and B segments. These interactions are characterized by the DPD parameters $a_{\alpha C}$ and $a_{\alpha D}$ ($\alpha = A, B$). It is expected that differences between the wetting properties of the C and D regions should influence the resulting equilibrium domain structures in the thin BCP film. We model the patterned substrate by assuming that two identical solid layers of immobile DPD particles are arranged in a regular array and stuck on the bottom boundary.

The interaction between DPD particles in our five-component system is the sum of three contributions: a repulsive conservative force, a dissipative force, and a stochastic force. The conservative force, $\mathbf{f}^{con}$, acts between pairs of DPD beads and takes into account their relative miscibility and the interaction between adjacent beads in the bead−spring model of a polymer chain. The dissipative force, $\mathbf{f}^{dis}$, acts as a heat sink and the random force, $\mathbf{f}^{ran}$, acts as a heat source (together the $\mathbf{f}^{dis}$ and $\mathbf{f}^{ran}$ forces act as a thermostat). The net force $\mathbf{F}$ applied on particle i is a sum of

25187

dx.doi.org/10.1021/jp204629k |J. Phys. Chem. C 2011, 115, 25185–25200

these three pairwise additive forces. The mesoscopic dynamics of the DPD particles are followed by solving the system of Newton's equations of motion, with the above forces.

As starting repulsive force parameters $a_{\alpha\beta}$ (α,β = A,B,C,D) in the conservative force, we used the parameters which were estimated by Scocchi at al. via mapping the corresponding energy values obtained from atomistic molecular dynamics simulations of polymer–clay nanocomposites.[69] The initial values of a_{AG} and a_{BG} were chosen to be $a_{AG} = a_{BG} = 50$, while all $a_{\alpha\beta}$ were fixed at $a_{\alpha\alpha} = 25$.[68] This initial set of parameters {$\mathbf{a}$} was systematically varied in a series of simulations in order to ensure the stability of the formed structures. The repulsion between the unlike particles is the driving force for phase separation. When the interactions between the unlike particles $a_{\alpha\beta}$ ($\alpha \neq \beta$) are close to $a_{\alpha\alpha}$, the phase separation takes place in the weak segregation regime, so that the structure formation is very slow. It is clear that choosing a larger difference $\Delta_{\alpha\beta}$ ($=a_{\alpha\beta}-a_{\alpha\alpha}$) can speed up the phase separation process. However, when the values of $\Delta_{\alpha\beta}$ are too large, some metastable structural distortions can be trapped in the domain formed by the other component in the early stage of simulation, and these trapped structural distortions are very difficult to be released. Thus, increasing the phase separation driving force will enhance the phase interfaces, which are very difficult to be broken at the simulation temperature. Consequently, the system may evolve into a trapped state instead of the equilibrium state. After several tries and errors with energy parameters, we set them as follows:

$$
a = \frac{k_B T}{\sigma}
\begin{pmatrix}
 & A & B & C & D & G \\
A & 25 & a_{AB} & 10 & 50 & 50 \\
B & & 25 & 50 & 10 & 50 \\
C & & & 25 & 25 & 50 \\
D & & & & 25 & 50 \\
G & & & & & 25
\end{pmatrix}
\tag{11}
$$

where a_{AB} is considered as a variable parameter; it was chosen to be $a_{AB} = 45$ in most of simulations discussed below. The set of parameters (11) supplies enough thermodynamic driving force for phase separation and is not too large to drastically trap the morphology evolution. Keeping the ratio between $a_{\alpha\beta}$ constant, we also systematically varied their values to estimate the critical point of phase transition and to monitor the pathways between different microstructures. To this end, we assumed that the total potential U depends on a continuous coupling parameter λ such that as λ is varied from 0 to 1, the values of $a_{\alpha\beta}$ change as $a_{\alpha\beta} = a_{\alpha\alpha} + \lambda\Delta_{\alpha\beta}$ and, therefore, U_λ passes smoothly from U_0 to U_1. A series of 32 simulations corresponding to successive discrete values of λ was carried out.

The interaction DPD parameters ($a_{\alpha\beta}$) can be linked to the χ-parameters in a Flory–Huggins-type model:[68] $\chi_{\alpha\beta} = 0.286\Delta_{\alpha\beta}$ at number density $\rho\sigma^3 = 3$. Later, Groot and Madden[70] found that for relatively short chains, most of the DPD simulations produce a phase structure predicted by the self-consistent field theory[5,6] when an effective Flory–Huggins parameter $\chi_{\alpha\beta}^{(eff)}$ is used. A rough estimate for the relation between $\chi_{\alpha\beta}^{(eff)}$ and $\chi_{\alpha\beta}$ is given by[70]

$$
\chi_{\alpha\beta}^{(eff)} = \frac{\chi_{\alpha\beta}}{1 + 3.9N^{-0.51}}
\tag{12}
$$

where N is the chain length.

The volume fractions of the polymer and the gas in the simulation box were chosen to be 0.8 and 0.2, respectively. Since the characteristic dimensions of the block copolymer domains are physically determined by the block lengths, the total chain length N should provide consistency with the characteristic size of the underlying pattern. Typically, in DPD simulations, the system was composed by n = 9451 AB diblocks (f = 0.25) of length N = 32 and n_G = 75645 G-particles. We note that Detcheverry et al.[49] used the same chain length in their TICG simulation. It is true that this chain length is rather short, but in order to simulate the periodic ordered structures of more than one period, we cannot take larger N, since the characteristic period of the resulting hexagonal phase becomes very large for long chains. The total number of the substrate particles was 8192. To avoid the penetration of polymer beads into the substrate, the substrate particles inside each layer are separated by a distance of $\sigma\rho^{-1/3}$ and the distance between the layers is $0.8\sigma\rho^{-1/3}$. The interacting forces between any pair of DPD particles were taken to be the same for both mobile and frozen (substrate) particles. In the course of the simulation, we did not update the positions of the substrate particles but in the calculation of the dissipative forces we attributed to those particles a velocity randomly selected from the Maxwell–Boltzmann distribution, corresponding to the target temperature T, to avoid the development of temperature gradients near the substrate.

In computer simulations of phase-separating systems, a fixed size of the simulation box entails the risk of suppressing or influencing the formation of particular structures. In an effort to avoid this effect, our DPD simulations were carried out at constant pressure and constant temperature. The temperature was maintained by the standard DPD thermostat[68] while the pressure was maintained by the Langevin piston algorithm.[71] The use of a constant pressure (isobaric) constraint in the simulations allowed box dimensions to change, thereby minimizing the effect of the box size on the final system morphology. Specifically, we used an extension of the standard NPT ensemble, viz., the NPAT (constant normal pressure, surface area and temperature) ensemble, which is the specific ensemble for thin films (all technical details are discussed in Appendix B). The choice of the NPAT ensemble is crucial for the success of the simulations. The pressure in the z direction, $P_{zz}^{(0)}$, was obtained in the course of preliminary long simulations in NVT ensemble for the system with target bead density $\rho\sigma^3$ = 3. With this external pressure, the overall average density of mobile DPD particles (A, B and G) in the simulation NPAT box was found to be very close to its target value. All the other parameters used in the simulations were taken from refs 68, 72, and 73.

Starting from a disordered state, to minimize kinetic trapping, we slowly changed the DPD force parameters (11) during the equilibration run, until they reached the values of interest $a_{\alpha\beta}$ and an ordered state was achieved. This simulation-annealing procedure followed the usual linear schedule,[73] $a_{\alpha\beta}^{(s)} = a_{\alpha\alpha} + (a_{\alpha\beta} - a_{\alpha\alpha})s/n_s$, where the initial values $a_{\alpha\alpha}$ were set to 25, $a_{\alpha\beta}^{(s)}$ are the force parameters at time step s, and n_s is the number of time steps, which was taken to be 4×10^6. This resulted in the development of long-range order in the polymer matrix, which persisted over the entire simulation box. This strategy is analogous to cooling a real BCP film across the order–disorder boundary. After the equilibration, we simulated systems at least for 2×10^6 time steps to compute the desired quantities at the predetermined values of $a_{\alpha\beta}$. The calculations were carried out in parallel using a highly optimized DPD code.

2.3. Patterns. Several types of patterns were constructed. A hexagonal pattern represents the projection of hexagonally

25188

dx.doi.org/10.1021/jp204629k |J. Phys. Chem. C 2011, 115, 25185–25200
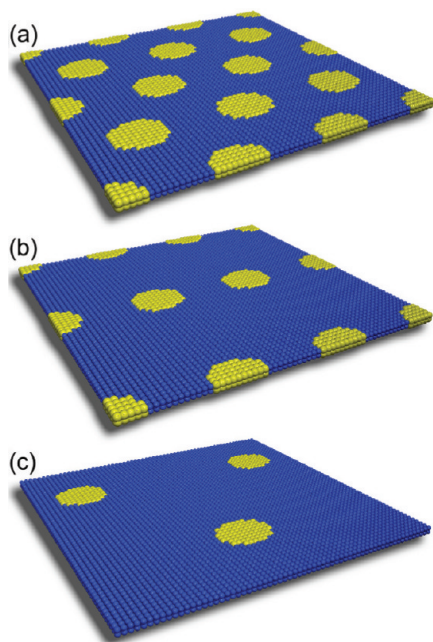
Figure 1. Patterned surfaces used in our simulations: (a) hexagonal pattern, (b) sparse rectangular pattern (SRP), and (c) sparse triangle pattern (STP). The substrate is composed of two types of sites, C and D, which experience different chemical affinities toward the A and B segments of a cylinder-forming AB diblock copolymer. During self-assembly, the minority A blocks preferentially wet the circular C spots and the majority B blocks preferentially wet the D regions. In the case of the hexagonal pattern, the periodicity of the A-like regions is equal to the period of the bulk hexagonal phase, d_0 (generic hexagonal pattern, GHP) or it can be $2d_0$ (sparse hexagonal pattern, SRP). For the SRP and STP, there are two characteristic length scales: $(d_0, \sqrt{3}d_0)$ and $(d_0, 2d_0)$, respectively. The fraction of the C sites, f_C, is fixed at $\pi/8\sqrt{3} = 0.2267$ (for GHP), $\pi/16\sqrt{3} = 0.1134$ (for SRP), and $\pi/32\sqrt{3} = 0.0567$ (for SHP and STP). These patterns are idealized analogues of the chemical surface patterns manufactured experimentally. The C regions preferentially wettable by the type A segments are given in yellow and the D regions preferentially wettable by the type B segments are given in blue.

arranged cylinder domains on the xy plane (Figure 1a). It is assumed that the resulting two-dimensional hexagonal array of circular spots contains the type C sites and the remaining background contains the type D sites. The spot size is approximately the same as the cylinder diameter. The fraction of the C-sites, f_C, was fixed at $f_C = \pi/8\sqrt{3} = 0.2267$ or at $f_C = \pi/32\sqrt{3} = 0.0567$. We will call these patters "generic hexagonal pattern" (GHP) and "sparse hexagonal pattern" (SHP), respectively. These two hexagonal patterns with a period of d_0 or $2d_0$ are commensurate with the unconfined hexagonal morphology in the bulk. The GHP matches perfectly the hexagonal packing of cylindrical domains of the bulk copolymer, but the SHP does not.

If even (or odd) rows of the type C spots are removed from the GHP, we obtain a "sparse rectangular pattern" (SRP) with $f_C = \pi/16\sqrt{3} = 0.1134$ and two characteristic length scales, d_0 and $\sqrt{3}d_0$ (Figure 1b). It should be noted that the SRP, which can be considered as a lower-spatial-frequency template, is also commensurate with the bulk hexagonal packing because the dimensions of its primitive rectangular cell are defined by the vector $(d_0, \sqrt{3}^{1/2}d_0)$. It is clear that the number of spots in the SHP and SRP is, respectively, one-quarter and one-half the number of spots in the GHP.
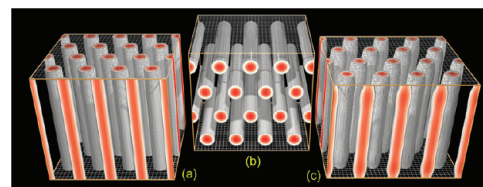
Figure 2. Typical examples of the hexagonally packed cylindrical domains observed in the SCFT calculations for the case of homogeneous confining walls: (a) perpendicular phase $C_\perp$ (the confining walls are neutral, $\varepsilon_A^{(b)} = \varepsilon_A^{(t)} = 0$ and $\varepsilon_B^{(b)} = \varepsilon_B^{(t)} = 0$); (b) parallel phase $C_\parallel$ (the minority-selective confining walls, $\varepsilon_B^{(b)} = \varepsilon_B^{(t)} = 0$ and $\varepsilon_A^{(b)} = \varepsilon_A^{(t)} \equiv \varepsilon_A = 0.6$) (c) perpendicular phase (the minority-selective confining walls, $\varepsilon_B^{(b)} = \varepsilon_B^{(t)} = 0$ and $\varepsilon_A^{(b)} = \varepsilon_A^{(t)} \equiv \varepsilon_A = 0.33$). For the case (c), undulational deformations of cylinder domains are observed under preferable film boundaries.

Additionally, in the DPD simulations, we used a "sparse triangle pattern" (STP), which has two characteristic length scales, d_0 and $2d_0$ (Figure 1c). This pattern with $f_C = 0.0567$ is also obtained from the generic hexagonal pattern. It should be stressed that the characteristic length scales of the GHP, SHP, and STP are integer multiplies of the natural block copolymer spacing, but for the SRP this is not the case. The patters used in the DPD simulations are shown in Figure 1.

3. RESULTS AND DISCUSSION

3.1. Homogeneous Confining Walls. To facilitate the discussion, we start with the SCFT calculations of a reference system with two homogeneous confining walls ($\varepsilon_A^{(C)} = \varepsilon_A^{(D)}$ and $\varepsilon_B^{(C)} = \varepsilon_B^{(D)}$) which repel the type A segments ($\varepsilon_A^{(b)} = \varepsilon_A^{(t)} \equiv \varepsilon_A > 0$) and are neutral to the majority component B ($\varepsilon_B^{(b)} = \varepsilon_B^{(t)} = 0$). This surface field plays a role of a chemical potential difference between the two species at the surfaces and corresponds to the so-called symmetric wetting conditions. Thus, for the reference system, there are only two independent variables, viz., h and ε_A.

As mentioned above, we are mainly interested in the relative stability of parallel ($C_\parallel$) and perpendicular ($C_\perp$) cylinder morphologies. Typical examples of these morphologies observed in the SCFT calculations for the case of neutral and selective confining walls are shown in Figure 2. The phase diagram of the reference system with two homogeneous confining walls is shown in Figure 3, where we present the results for the films with the thickness up to five parallel cylinder layers ($C_\parallel^{(m)}$, $m = 5$, where m is an integer number).

As seen in Figure 3, for small ε_A ($0 < \varepsilon_A \lesssim 0.33$) the $C_\perp$ phase is stable over the whole range of h. For larger ε_A, the $C_\perp$ phase becomes unstable and transforms into the $C_\parallel^{(m)}$ phase when the slit width h is close to $\sqrt{3}md_0/2$. This transformation takes place because the free energy gain caused by the selectivity of the confining walls exceeds the free energy loss caused by cylinder deformations near the film boundaries (for more detail, see below). When h deviates essentially from $\sqrt{3}md_0/2$, the $C_\perp$ phase is stable. However, an increase of ε_A drastically stabilizes the parallel phase. Generally, these results are in agreement with the earlier calculations of the phase diagrams of asymmetric block copolymers using dynamic density functional theory (DDFT)[16,23,74,75] and with SCFT calculations of Matsen,[58] who used, however, a different parameter set.

We note that when the film thickness is equal to the distance between cylinder axes in the bulk and $\varepsilon_A = 0$, the $C_\parallel$ phase with its

25189

dx.doi.org/10.1021/jp204629k |*J. Phys. Chem. C* 2011, 115, 25185–25200
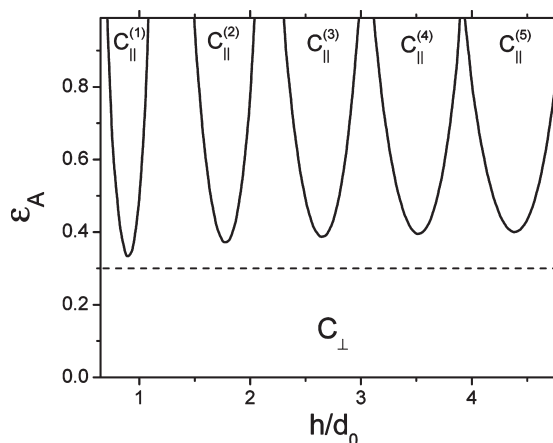
Figure 3. Phase diagram of a diblock AB copolymer melt in a slit with homogeneous confining walls separated by a distance h, at $\chi N = 20$. The bottom and top confining walls are repulsive for the minority component A ($\varepsilon_A^{(b)} = \varepsilon_A^{(t)} \equiv \varepsilon_A > 0$) and neutral for the majority component B ($\varepsilon_B^{(b)} = \varepsilon_B^{(t)} = 0$). The region, where the perpendicular phase is stable, is denoted as $C_\perp$. The regions, where the parallel phase is stable, are denoted as $C_\parallel^{(m)}$ (m is the number of cylinder layers). The region of strongly deformed perpendicular cylinders (cf. Figure 2c) is located above the dashed horizontal line.

cylinder axes lying on the surface in the wall layers (the $C_{\parallel a}$ phase in the notation of Matsen, see Figure 1a from ref 58) has the same free energy as the $C_\perp$ phase. But this very special point in the phase diagram is an "isolated point" (where a phase transition of a special kind, second-order phase transition, occurs) and therefore the corresponding states are unstable. At $\varepsilon_A > 0$, the free energy of the $C_\perp$ phase is always lower than that of the $C_{\parallel a}$ phase. The reason for this is easily understood from simple geometric estimates. Indeed, the fraction of contacts between the minority component and the surface cannot be greater than 0.25 for perpendicular cylinders, while for the $C_{\parallel a}$ phase, this value is 0.525. Therefore, with increasing ε_A, only the $C_\perp$ phase or an alternative parallel morphology with cylinders that are close to, but do not touch, the surface (the $C_{\parallel b}$ phase in the notation of Matsen, see Figure 1b from ref 58) can be stable.

From the analysis of density fields, we find that perpendicular cylinders become deformed gradually when the parameter ε_A is increased (cf. Figure 2c). The dashed horizontal line in Figure 3 at $\varepsilon_A \approx 0.3$ delimits the region where the cylinders are weakly deformed ($\varepsilon_A < 0.3$) and the region of stronger deformations ($\varepsilon_A > 0.3$).

The free energy per polymer chain F as a function of the film thickness h for the reference system with the confining walls preferring to contact only the majority B segments is displayed in Figure 4. The free energy F of confined $C_\perp$ phase monotonically decreases with increasing h. The curves corresponding to the parallel phase $C_\parallel^{(m)}$ intersect the curve predicted for the $C_\perp$ phase around the local free energy minima for the $C_\parallel$ phase at $h \approx \sqrt{3}md_0/2$ which are the stability regions of the $C_\parallel$ phase. A transition in the number of layers from m to $m + 1$ ($C_\parallel^{(m)} \rightarrow C_\parallel^{(m+1)}$) is expected to occur at $h \approx \sqrt{3}(m + 0.5)d_0/2$. Therefore, the confined BCP film of given h should select the optimum value of m with the lowest F. Note that in reality, when small thermal fluctuations are possible, one can expect a coexistence of $C_\parallel^{(m)}$ and $C_\parallel^{(m+1)}$ structures at sufficiently large m for certain film thickness around $\sqrt{3}(m + 0.5)d_0/2$.
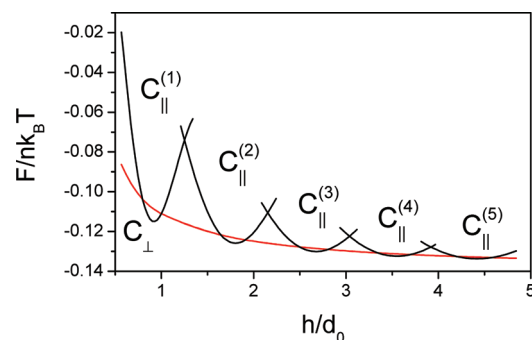

Figure 4. Free energy per polymer chain of the $C_\perp$ and $C_\parallel^{(m)}$ structures as a function of the reduced film thickness h at $\chi N = 20$. The bottom and top confining walls are identical and homogeneous. They are neutral for the type B segments ($\varepsilon_B^{(b)} = \varepsilon_B^{(t)} = 0$) and weakly repulsive for the type A segments ($\varepsilon_A^{(b)} = \varepsilon_A^{(t)} \equiv \varepsilon_A = 0.5$). The local free energy minima for the $C_\parallel^{(m)}$ phase are observed at $h \approx \sqrt{3}md_0/2$, where m is the numbers of parallel cylinder layers.

In thicker films, the difference between the free energies of the $C_\perp$ and $C_\parallel$ phases is gradually decreasing so that at $h \gtrsim 4d_0$ our calculations predict two coexisting phases. Such behavior is characteristic of the unconfined case when the cylinder orientation is selected randomly (since the system is isotropic) and BCPs tend to phase separate into a microscale multigrain structure. Nevertheless, our results demonstrate that the $C_\parallel$ phase can prevail for certain h even in very thick films. On the other hand, the perpendicular morphology can evidently achieve a lower free energy if the film thickness is not compatible with the bulk lattice period or the interactions of the A and B blocks with the confining walls are balanced, making the wall surfaces "effectively neutral" so chains are not favored to spread out on the surfaces. From simulations it is known that in order to make the surfaces "effectively neutral" for asymmetric copolymers, slight preferential wetting of the surfaces for the majority block is required.[76−79] Under these conditions, the entropic preference of a neutral surface for the shorter block (due to the enrichment of chain ends near hard surfaces) is compensated by the energetic preference of the surface for the majority block. This situation can, in principle, be realized in practice on a substrate modified with a random copolymer.[80] For example, the results of Han et al.[81] have revealed perpendicular orientation of long cylindrical domains in PS-b-PMMA block copolymer on cross-linked random copolymer layers which are similar to the substrates with slight preference to the majority block in the simulations.

It should be noted that when the confining walls attract the minority A-blocks, the formation of lying cylinders as well as half-cylinders is typically observed near the walls[58,76−79] Thus we conclude that the equilibrium self-assembled morphology in thin BCP films is controlled not only by the ratio between the film thickness and the bulk cylinder spacing, but also largely by the polymer-surface interaction. We note also that when the film boundaries strongly prefer one of the components of a diblock copolymer, the formation of parallel phase oriented along the substrate always takes place. Furthermore, the experimental data show that in this case, BCP films often split in neighboring terraces of different thickness and microdomain orientations.[23,25,82,83] In the next subsection, we will turn to the effect of chemically patterned substrates and seek recipes to further stabilize the perpendicular arrangement of cylindrical domains.

Generally, the reference system behaves in agreement with the earlier theoretical[58,76−79] and experimental[23,25,82,83] studies

25190

dx.doi.org/10.1021/jp204629k |*J. Phys. Chem. C* 2011, 115, 25185–25200
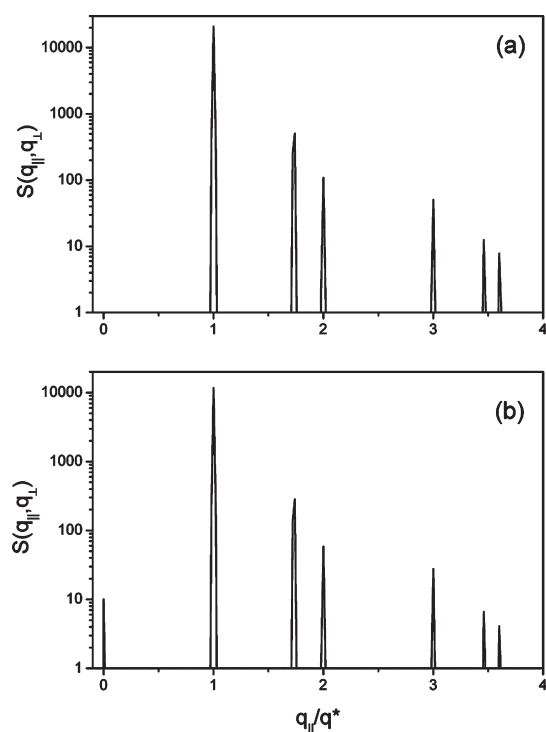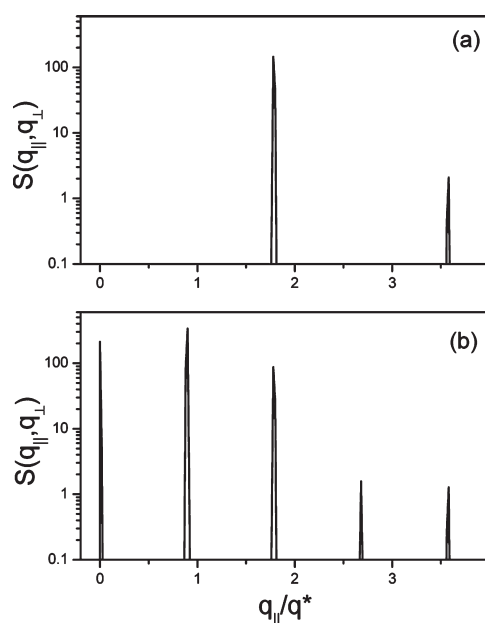
Figure 5. Circularly averaged structure factor $S(q_\parallel, q_\perp)$ for the $C_\perp$ phase as a function of the lateral wavenumber $q_\parallel$ at $q_\perp/q^* = 0.1$, where q^* is the position of the main (first-order) peak. (a) The symmetric wetting conditions, when both film boundaries are homogeneous and neutral ($\varepsilon_A^{(b)} = \varepsilon_A^{(t)} = 0$ and $\varepsilon_B^{(b)} = \varepsilon_B^{(t)} = 0$). (b) The bottom and top confining walls are neutral for the type B segments ($\varepsilon_B^{(b)} = \varepsilon_B^{(t)} = 0$) and weakly repulsive for the type A segments ($\varepsilon_A^{(b)} = \varepsilon_A^{(t)} \equiv \varepsilon_A = 0.5$). The degree of segregation is fixed at $\chi N = 20$.

Figure 6. Circularly averaged structure factor $S(q_\parallel, q_\perp)$ for the $C_\parallel^{(4)}$ phase as a function of lateral wavenumber $q_\parallel$ at (a) $q_\perp/q^* = 0$ and (b) $q_\perp/q^* = 0.1$, where q^* is the position of the main (first-order) peak. The degree of segregation is fixed at $\chi N = 20$.

which showed that the equilibrium self-assembled morphologies and the degree of the translational and orientational order in thin BCP films are largely controlled by the polymer-surface interactions.

In order to obtain additional information about the effect of confining walls on the shape of microdomains, we carried out reciprocal space analysis of nanostructured polymer films by calculating scattering intensities of the static structure factor. In experiments, such analysis is a widespread technique to determine the density profile perpendicular to the film surface. The formal definition of the structure factor $S(q_\parallel, q_\perp)$ ($q_\parallel$ and $q_\perp$ being the lateral and normal wave numbers, respectively) is given in Appendix A (eqs A3 and A5).

First, we examine an "ideal" $C_\perp$ morphology (Figure 2a) for the symmetric wetting conditions, when both film boundaries are homogeneous and neutral ($\varepsilon_A^{(b)} = \varepsilon_A^{(t)} = 0$ and $\varepsilon_B^{(b)} = \varepsilon_B^{(t)} = 0$). Because the confining walls in our model behave as reflecting boundaries, the $C_\perp$ structure is completely equivalent to the bulk cylinder phase. Obviously, for this system, the density distribution of different polymer segments depends only on the lateral (x, y) coordinates. Therefore the $S(q_\parallel, q_\perp)$ function shown in Figure 5a depends only on the lateral wavenumber $q_\parallel$ and is not dependent on the normal component $q_\perp$. The absolute value of the wave vector belonging to the main harmonics is given by $q^* = 4\pi/\sqrt{3}d_0$. The peak positions correspond to a hexagonal lattice ($q_\parallel/q^* = 1, \sqrt{3}, \sqrt{4}, \sqrt{7}, \sqrt{9}, (11)^{1/2}, \ldots$), as expected. The cylinders of the $C_\perp$ phase can change their shape when the confining walls are preferable for the majority B-block

(cf. Figure 2c). These deformations are reflected in the structure factor shown in Figure 5b. It is seen that an additional peak arises at $q_\parallel/q^* = 0$. This peak is associated with the harmonics $(0,0,q_\perp)$, which are responsible for such deformations. Strictly, the A-rich domains are not cylindrical when the confining walls repel (or attract) one of the blocks. Under these conditions, they become modulated in the z-direction. Hence, the structure factor reflects the selectivity of the film boundaries.

The structure factor changes dramatically for $C_\parallel$ phase as compared to $C_\perp$ phase. As follows from the geometry of the $C_\parallel$ phase (cf. Figure 2b), the $S(q_\parallel, q_\perp)$ function always depends on both $q_\parallel$ and $q_\perp$. As an example, we present in Figure 6 the structure factor for $C_\parallel^{(4)}$ phase in the small-angle scattering regime $q_\perp/q^* \ll 1$, at $q_\perp = 0$ and 0.1. For these values of $q_\perp$, the $S(q_\parallel, q_\perp)$ function describes the scattering from 2D orthogonal projection of the $C_\parallel^{(4)}$ phase onto the substrate plane (Figure 6a) and from 3D parallel structure, which is characterized by a double number of peaks in comparison with the 2D orthogonal projection (Figure 6b). The additional peaks in Figure 6b reflect the presence of harmonics with nonzero $q_\perp$. In particular, the peak observed at $q_\parallel = 0$ corresponds to the harmonics $(0,0,q_\perp)$. Indeed, even and odd layers of cylinders are not distinguishable in the 2D orthogonal projection, thus the lateral period of this projection is two times smaller than that of the volume $C_\parallel^{(4)}$ phase. As seen in Figure 6, the peaks are approximately equidistant. This fact reflects a lamella-like nature of the lateral structure of $C_\parallel$ phase. The main (most intense) peak in Figure 6b is located at $q_1 = \sqrt{3}d_0 q^*/2d_\parallel \cong 0.904q^*$, where $d_\parallel$ is the period of $C_\parallel$ phase and d_0 is the natural period in the bulk. Thus, the structure factor of $C_\parallel$ phase in a thin-film geometry gives useful information about the period deviation in comparison to the bulk hexagonal packing. In our case, we find that $d_\parallel < d_0$. It should be noted that the change in the number of cylinder layers weakly affects the structure factor, and the period
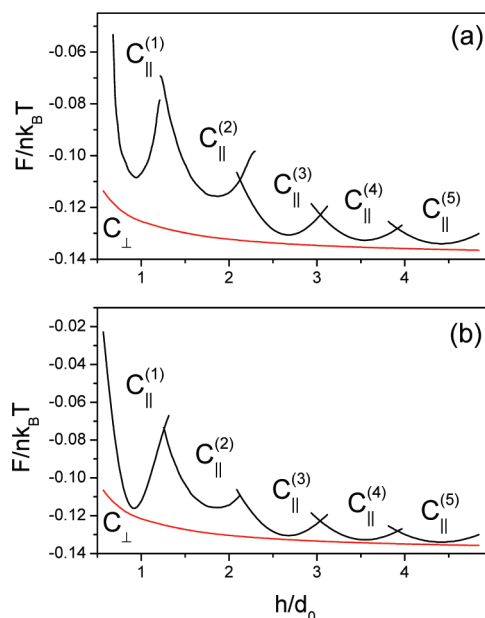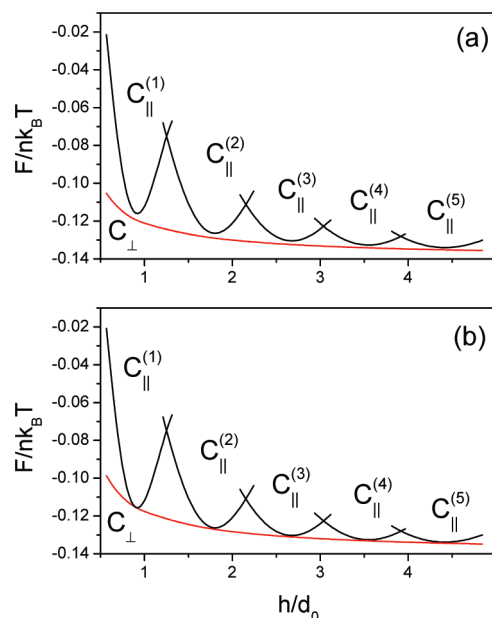
Figure 7. Free energies of perpendicular $(C_\perp)$ and parallel $(C_\parallel^{(m)})$ hexagonal phases confined between two impenetrable walls as a function of film thickness h in the presence of the hexagonal pattern (cf. Figure 1a). The confining walls and the sites of the substrate pattern are neutral for the majority B blocks, $\varepsilon_B^{(b)} = \varepsilon_B^{(t)} = 0$ and $\varepsilon_B^{(C)} = \varepsilon_B^{(D)} = 0$. The minority A blocks have repulsive interactions of strength $\varepsilon_A^{(t)} = \varepsilon_A^{(D)} = 0.5$ with the top wall and with the D sites of the substrate pattern and attractive interaction of strength $\varepsilon_A^{(C)} < 0$ with the C sites of the substrate pattern: (a) $\varepsilon_A^{(C)} = -0.5$ and (b) $\varepsilon_A^{(C)} = -0.25$. The degree of segregation is fixed at $\chi N = 20$.

Figure 8. Free energies of perpendicular $(C_\perp)$ and parallel $(C_\parallel^{(m)})$ hexagonal phases confined between two impenetrable walls as a function of film thickness h in the presence of the sparse rectangular pattern (SRP) shown in Figure 1b. The confining walls and the sites of the substrate pattern are neutral for the majority B blocks, $\varepsilon_B^{(b)} = \varepsilon_B^{(t)} = 0$ and $\varepsilon_B^{(C)} = \varepsilon_B^{(D)} = 0$. The minority A blocks have repulsive interactions of strength $\varepsilon_A^{(t)} = \varepsilon_A^{(D)} = 0.5$ with the top wall and the D sites of the substrate pattern and attractive interaction of strength $\varepsilon_A^{(C)} < 0$ with the C sites of the substrate pattern: (a) $\varepsilon_A^{(C)} = -1.0$ and (b) $\varepsilon_A^{(C)} = -0.5$. The degree of segregation is fixed at $\chi N = 20$.

of $C_\parallel$ phase, $d_\parallel$, approaches the period in the bulk d_0 with film thickness increasing.

3.2. Effect of Substrate Patterns in SCFT Simulations. The use of the periodic surface field $\gamma_\alpha(\mathbf{r})$ in eq 6 makes the present system different from that of previous theoretical (SCFT) studies (see, e.g., refs 58 and 84−90,), where the two surfaces were identical and homogeneous. In our fully three-dimensional calculations only one (top) surface is homogeneous whereas the bottom surface contains a chemical pattern. In their SCFT calculations, Kim at al.[91] used a stripe-like pattern to guide self-assembly of cylinder-forming copolymers, but they did not study the effect of pattern multiplication. In our SCFT calculations, the energy parameters describing the interactions between polymer segments and confining walls were chosen according to their previous evaluation in refs 58, 89, 92, and 93.

In order to find the most stable state of the film in the presence of chemically patterned substrates, we again calculate and compare the free energy of the $C_\perp$ and $C_\parallel$ phases for different h. The SCFT results obtained with the hexagonally patterned substrate (the GHP pattern) are shown in Figure 7. We set $\varepsilon_A^{(D)} = 0.5$, as before, but now we introduce a preferential wetting of the pattern spots by the minority A-blocks ($\varepsilon_A^{(C)} = -0.5$ or -0.25). A comparison of these results with those shown in Figures 3 and 4 makes evident a significant enhancement of the relative stability of the $C_\perp$ phase. The imposition of the surface pattern decreases F because of a rearrangement of the spatial distribution of the chain segments near the substrate. As seen in Figure 7, for a wide range of h, the free energy of the $C_\perp$ phase can be significantly lower than that predicted for the $C_\parallel$ phase when there is even rather weak affinity between the minority domains and the
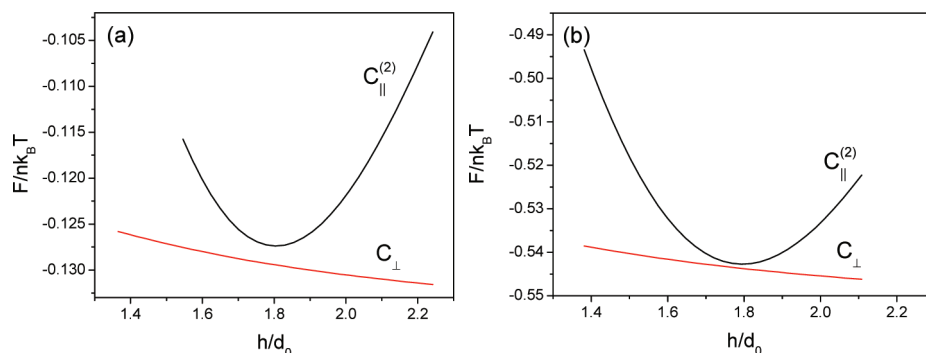
pattern ($\varepsilon_A^{(C)} = -0.25$). In the presence of the pattern, the $C_\parallel$ phase becomes metastable or completely unstable for any realistic values of h. The pattern effect on the film ordering weakens for large h, as expected.

From a general viewpoint, the equilibrium morphology of BCPs interacting with a patterned substrate should be the result of the competition between the following three contributions to the system free energy: (1) the monomer−monomer interactions, (2) the polymer-pattern interactions, and (3) the entropic cost of stretching chains in the segregated state.[94] The pattern effect on the equilibrium morphology can, in principle, be either local or global. Qualitatively, the polymer-pattern interaction is related to the local density profile of the monomers near the pattern (surface energy). Intuitively, the equilibrium state of the BCP film should be affected only in the vicinity of the substrate so that the pattern's effect on the distribution of the BCP components should quickly decay in the interior of the film. However, we have shown that the resulting effect of the substrate pattern which is commensurate with the copolymer morphology in the bulk is evidently global in the sense that it propagates throughout the whole film volume. It stands to reason that both the domains registration and the preferable orientation of BCP microdomains strongly depend on the pattern geometry and on the surface fields.

Let us now consider what happens when the same BCP film interacts with sparse patterns (SRP and SHP) which have two different characteristic length scales. Note that SRP does not coincide with the bulk repeat period of the copolymer as it contains only a half of the attractive sites as compared to the

Figure 9. Free energy of $C_\perp$ and $C_\parallel^{(2)}$ phases as a function of slit thickness h in the presence of the sparse hexagonal pattern (SHP) with a period of $2d_0$, at (a) $\chi N = 20$ and (b) $\chi N = 25$. The confining walls and the sites of the substrate pattern are neutral for the majority B blocks, $\varepsilon_B^{(b)} = \varepsilon_B^{(t)} = 0$ and $\varepsilon_B^{(C)} = \varepsilon_B^{(D)} = 0$. The minority A blocks have repulsive interactions of strength (a) $\varepsilon_A^{(t)} = \varepsilon_A^{(D)} = 0.5$ and (b) $\varepsilon_A^{(t)} = \varepsilon_A^{(D)} = 0.8$ with the top wall and with the D sites of the substrate pattern. The patterned C-spots are preferentially wet by the type A segments: (a) $\varepsilon_A^{(C)} = -1.5$ and (b) $\varepsilon_A^{(C)} = -1.0$.

"dense" hexagonal pattern (Figure 1). Therefore, in order to compare the effect of GHP and SRP, the energy parameter $\varepsilon_A^{(C)}$ should be twice larger in the case of SRP. The free energy per chain F as a function of h for $C_\perp$ and $C_\parallel$ phases is presented in Figure 8.

Again, we observe that the free energy predicted for the $C_\perp$ phase monotonically decreases as h increases, whereas for the $C_\parallel$ phase we find a sequence of multiple local minima with decreasing function values. The comparison of the free energies indicates that for the explored region of parameters, the parallel orientation does not survive. Therefore we conclude that when the pattern field is chosen such that the preferential wetting takes place between the C sites and the minority domains, the rectangular substrate pattern induces the stability of perpendicular phase whereas the parallel phase is metastable for all range of the film thickness considered. More importantly, the SRP directs the formation of a "dense" (or high-spatial-frequency) array of hexagonally arranged cylinders and doubling the frequency of the initial pattern. Such behavior is associated with the pattern interpolation process.

Next, we discuss the effect of the sparse hexagonal pattern (SHP) which contains only one-fourth of attractive spots of the GHP and which period is accordingly twice the natural cylinder period. Note that BCP self-assembly on such hexagonal array of spots has experimentally been investigated by Ruiz et al.[37] For the following discussion of the SCFT-based calculations, we restrict ourselves by considering the BCP films whose thickness does not exceed $\sim 3d_0$.

In Figure 9, we compare the free energy per chain of $C_\perp$ and $C_\parallel^{(2)}$ structures as a function of h at two degrees of segregation, $\chi N = 20$ (Figure 9a) and $\chi N = 25$ (Figure 9b). The free energy of the structure with parallel-oriented cylinders attains a minimum value at $h/d_0 \approx 1.8$. However, the $C_\perp$ phase has a lower free energy than $C_\parallel^{(2)}$ at any film thickness for the energy parameters $\varepsilon_A^{(C)}$ used in these calculations ($\varepsilon_A^{(C)} = -1.5$ at $\chi N = 20$ and $\varepsilon_A^{(C)} = -1.0$ at $\chi N = 25$).

Therefore, we evaluated the minimum (by modulus) value of $\varepsilon_A^{(C)}$ at which the $C_\perp$ phase at $h/d_0 = 1.8$ becomes more stable than $C_\parallel^{(2)}$. Figure 10 shows F as a function of $\varepsilon_A^{(C)}$ at $h/d_0 = 1.8$ and $\chi N = 20$. We find that a net free-energy gain is achieved when $\varepsilon_A^{(C)} \leq -0.7$, which corresponds to a weak attraction. Nearly the same result is obtained for stronger degree of segregation ($\chi N = 25$).

Our results demonstrate that the guided BCP self-assembly by sparse hexagonal patterns leads to the formation of the vertically
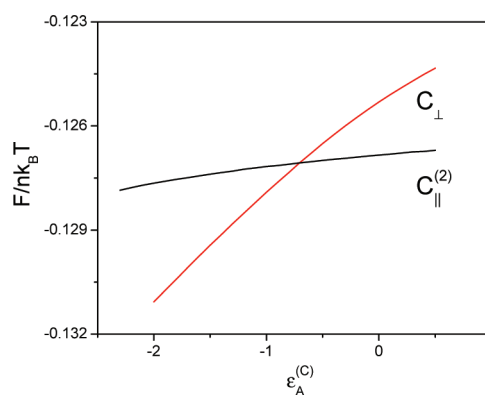

Figure 10. Free energy of $C_\perp$ and $C_\parallel^{(2)}$ structures interacting with the sparse hexagonal pattern as a function of the energy parameter $\varepsilon_A^{(C)}$ at $h/d_0 = 1.8$ (this distance corresponds to the free energy minimum of the $C_\parallel^{(2)}$ structure, as seen in Figure 9a). The confining walls and the sites of the substrate pattern are neutral for the majority B blocks, $\varepsilon_B^{(b)} = \varepsilon_B^{(t)} = 0$ and $\varepsilon_B^{(C)} = \varepsilon_B^{(D)} = 0$. The minority A blocks have repulsive interactions of strength $\varepsilon_A^{(t)} = \varepsilon_A^{(D)} = 0.5$ with the top wall and with the D sites of the substrate pattern. The degree of segregation is fixed at $\chi N = 20$.

oriented cylinder array whose density is increased by a factor of 4 since the pattern pitch is halved in both the x and y directions. The same interpolation effect has been experimentally observed by Ruiz et al.[37] and Yang et al.[42]

We used the structure factor to estimate quantitatively the effect of substrate pattern on the segment density distribution in the film volume. Shown in Figure 11 is the structure factor which was calculated for the $C_\perp$ and $C_\parallel^{(4)}$ phases formed on the substrate which contains the generic hexagonal pattern. The energy parameters and film thickness ($h/d_\parallel \approx 3.5$) correspond to the free energy minimum predicted for the $C_\parallel^{(4)}$ phase (cf. Figure 4). The most important observation is the presence in $S(q_\parallel, q_\perp)$ of the small satellite peaks close to the main peak at $q_\parallel/q^* \approx 1$. The appearance of these peaks in the spectra is a direct manifestation of the polymer-pattern interaction resulting in the deformation of cylindrical domains. However, the amplitudes of these peaks are relatively small (the ratio of their heights to the main peaks is of the order of 10^{-7}–10^{-5}) so it may well be that their experimental detection is hardly feasible.

3.3. Effect of Substrate Patterns in DPD Simulations. The model used in our DPD simulations represents a binary blend of
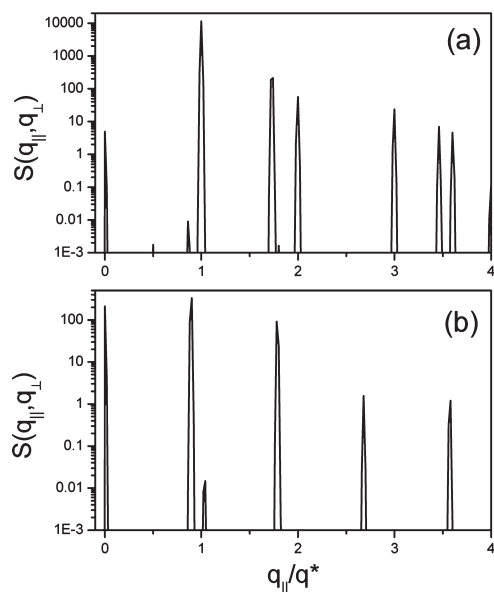
Figure 11. Circularly averaged structure factor $S(q_\parallel, q_\perp)$ for (a) $C_\perp$ phase and (b) $C_\parallel^{(4)}$ phase in the presence of the hexagonal pattern shown in Figure 1a, at $q_\perp/q^* = 0.1$, $\varepsilon_A^{(C)} = -0.5$, and $h/d_0 = 3.52$. The degree of segregation is fixed at $\chi N = 20$.

Figure 12. Per-bead variance of the total potential energy as a function of coupling parameter λ for the systems with three different patterns. The arrow specifies the region of microphase separation in the polymer matrix.

AB diblocks, which dominate in the blend, and type G particles. These components interact with one another and with patterned substrate. The self-assembly of the diblocks is driven by the immiscibility of their segments, so that we expect to find a segregated structure in the interior of the film. A number of phase-separation possibilities can occur depending on the inter-action between the components present in the system; examples are homogeneous mixtures, macroscopic phase separation, microscopic phase separation and the formation of different mesophases. When the blend contains a sufficient concentration of the AB copolymers, the result in the film interior should be a macroscopic phase separation into AB-rich and G-rich regions followed by microphase separation within the copolymer-rich domain into A-rich and B-rich subdomains. Such a process represents so-called "double phase separation" (DPS). The under-lying mechanism for this process, while seemingly intuitively obvious, remains poorly understood (see, e.g., refs 73, 95, and 96).

Possible structural transitions were characterized by monitor-ing the variation of thermodynamic and geometric properties over a range of coupling parameter λ from zero to unity. We begin by examining films in which all the DPD interaction parameters $a_{\alpha\beta}$ ($\alpha \neq \beta$) are changed simultaneously. To quantify the structural transitions that occur in the system, we consider the fluctuation (or variance) of the total potential energy U by computing

$$\delta U = (\langle U^2 \rangle - \langle U \rangle^2) \qquad (13)$$

We note that δU is proportional to the heat capacity defined as $(\langle U^2 \rangle - \langle U \rangle^2)/(nNk_BT)^2$.

The reduced variance δU per bead is shown in Figure 12 as a function of λ for the parameter set (11) with $a_{AB} = 40$ for the three systems with different types of surface patters. As is clearly evident from the figure, δU demonstrates sharp peaks that signal a transition. The peaks in these finite systems exhibit a one-sided
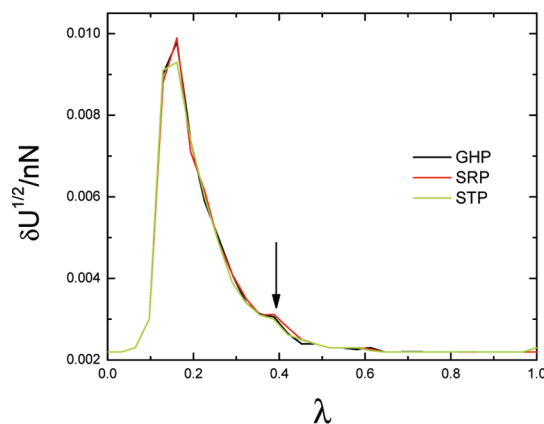
shape (being very steep on the small λ side of the transition). Although the scattering of δU in the vicinity of the transition is rather large, it is seen that the data points nearly collapse onto a single curve and the peaks are practically located at the same characteristic value $\lambda^* \approx 0.18$ (or $N\chi_{AB}^{(eff)} \approx 15$) for the three systems under discussion. The δU value at transition, λ^*, as determined by the location of the first maximum of δU, is also almost the same for these systems.

Visual inspection of a series of snapshots reveals that this transition is associated with the macrophase separation of the polymer chains and G-particles. Analogous conclusion can be drawn from the analysis of the density profiles $\rho_\alpha(z)$ in the direction perpendicular to the surface. They are shown in Figure 13 for the type A beads. It is seen that at small λ, the A beads are distributed more-or-less uniformly over the simulation box whereas, when λ is sufficiently large, there is a rather sharp interface between the polymer and gas phase in the upper region of the simulation box. Because of the high intensity of the first peak, we were unable to locate the second peak which is expected to be consistent with the order-disorder (ODT) transition in the polymer matrix. Analysis of the density profiles $\rho_A(z)$ and snapshots can help to understand the behavior of the model. Our simulations showed that in the range $0.4 \lesssim \lambda \lesssim 0.6$, the $\rho_A(z)$ functions demonstrate well-pronounced oscillations, particularly noticeable near the polymer-gas interface (cf. Figure 13). This means that in the polymer matrix, there exist A-rich and B-rich microdomains oriented mainly parallel to the interface. Under these conditions, however, one can observe the formation of perpendicular cylinders in the vicinity of patterned substrates (cf. Figure 14). As seen, the cylinders exhibit tilt and structural defects, and some of them are connected to each other in the plane of the film. As the parameter λ further increases, the density oscillations are damped and the density profiles $\rho_A(z)$ again smooth out when λ is close to 1 (Figure 13). In this case, a perpendicular orientation of the cylindrical microdomains is achieved through the full thickness of the film.

From the results discussed above, we conclude that the polymer matrix switches from the disordered state to an ordered cylinder morphology as $N\chi_{AB}^{(eff)}$ is stepped from ~26 to ~32. Therefore, the ODT window in our simulations is roughly between $a_{AB} = 29.8$ and 31 when $a_{AA} = a_{BB} = 25$. It should be noted that the segregation of A and B segments begins deep in
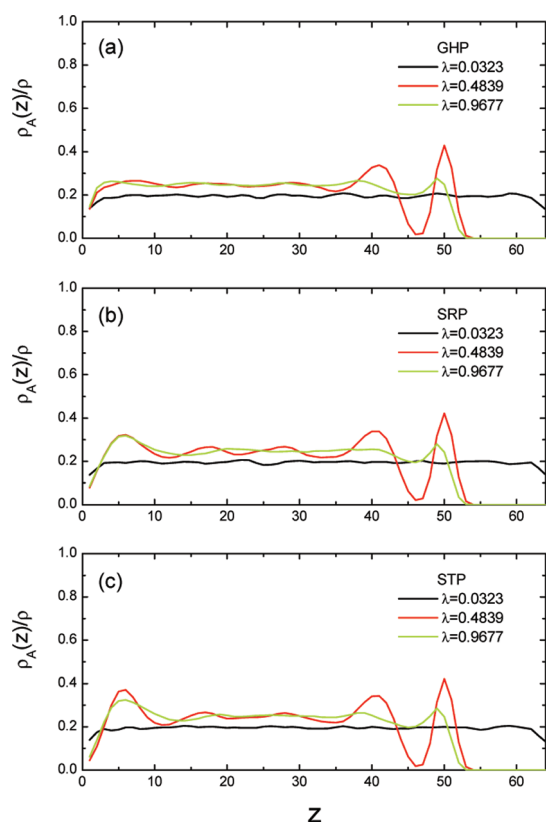
Figure 13. Normalized density profiles for the type A beads of the copolymer chains in the direction perpendicular to the substrate for the films interacting with (a) generic hexagonal pattern (GHP), (b) sparse rectangular pattern (SRP), and (c) sparse triangular pattern (STP), at different values of coupling parameter λ.
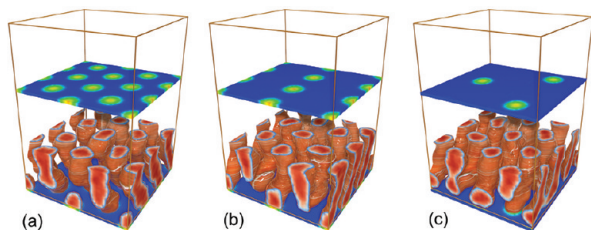
Figure 14. Representative snapshots from the DPD simulations illustrating the structure of the film in the vicinity of different patterned substrates in the intermediate segregation regime ($\lambda = 0.4839$, $N\chi_{AB}^{(eff)} = 39.4$): (a) generic hexagonal pattern (GHP), (b) sparse rectangular pattern (SRP), and (c) sparse triangle pattern (STP). Shown are the isodensity surfaces $\rho_A(\mathbf{r})/\rho_A = 1/2$ at $z \leq 20$, where ρ_A is the average density of A-beads. In our analysis of the simulation data we divided the system into an arbitrary number of cubic voxels. For each of the voxels the local density of beads, $\rho_A(\mathbf{r})$, was computed. Comparing local densities, interfacial voxels can be assigned that border regions of low and high density. For visual clarity we additionally show the patterned substrates near the middle of the simulation box.

the disordered region, as evident from the analysis of snapshots, but this effect is difficult to demonstrate, particularly in a quantitative manner. The estimated position of the ODT differs from that predicted in our SCFT calculations ($N\chi = 16.6$). This fact is not unexpected taking into account the differences between the two models (in particular, the SCFT model represents
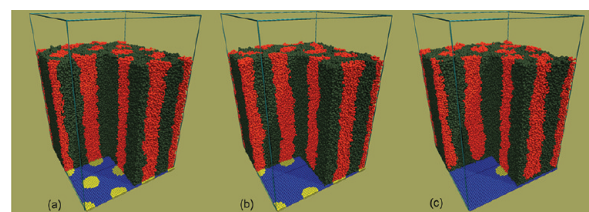

Figure 15. Representative snapshots from the DPD simulations illustrating the microphase-separated systems on different patterned substrates in the strong segregation regime: (a) generic hexagonal pattern (GHP), (b) sparse rectangular pattern (SRP), and (c) sparse triangle pattern (STP). A beads are given in red, B in dark-gray, C in yellow, and D in blue. For visual clarity, the type G particles, which occupy the upper region of the simulation box, are not shown and a part of the system is removed. The A-rich cylinders are connected directly to the complementary C-spots on the hexagonal pattern. Because the hexagonal pattern produces a periodic field with proper wavelength, all A-beads are totally registered along the A-preferring C-spots, and the B-beads are totally registered along the D-regions. The morphology of the film is highly ordered in both horizontal and vertical directions. In the case of the SRP and STP, the minority cylinder domains stand perpendicular to the surface of the substrate on the wetable sites C as well as in between the sites C. As a result, doubling and quartering the pattern frequency is observed for the resulting array of microdomains. This means that copolymer self-assembly on these chemical templates generates more features than were in the template itself.

the $N \rightarrow \infty$ limit and ignores polymer density fluctuations, as has been mentioned).

Next we examine films with well-separated domains. Under the strong segregation condition corresponding to the parameter set (11) with $a_{AB} = 45$, the guided phase-separation process modeled by the DPD simulations results in the formation of a well-organized structure where all vertical cylinders are 6-fold coordinated. As seen from the snapshot in Figure 15a, there are no cylinders with five or seven neighbors. The array of vertically oriented cylinders ("cylindrical brush") is formed in almost precise register with the underlying hexagonal pattern so that the pattern period is replicated with great fidelity and the pattern motif is transferred into the bulk material. In order to test the robustness of the observed structures, at least three different initial configurations were used. Good reproducibility of the resulting morphologies was obtained.

From the visual inspection of the snapshots similar to those shown in Figure 15 we infer that in the upper part of significantly thick films (close to "free" surface), the cylinders can slightly change their orientation near average packing positions (slow librations with low amplitude). In particular, the cylinders can exhibit slight tilt or structural defects. This is due to the fact that in the segregation regime considered here ($a_{AB} = 45$ or $\chi_{AB}^{(eff)} \approx 3.36$ and $N\chi_{AB}^{(eff)} \approx 107.5$), the interfaces between A and B domains fluctuate rather strongly due to thermal noise.

In order to access in more detail the quality of the pattern replication, we analyzed cross sections of the $C_\perp$ phase at different z (Figure 16). The data demonstrate a well-pronounced pattern transfer effect: the A-rich regions in the interior of the film practically coincide with the circular C-regions "written" on the pattern (cf. Figures 1a and 16, left panels). Therefore, even in the intermediate segregation regime the complementary heterogeneous motif on the substrate can be transferred into the bulk almost completely, although we expect the quality of the pattern
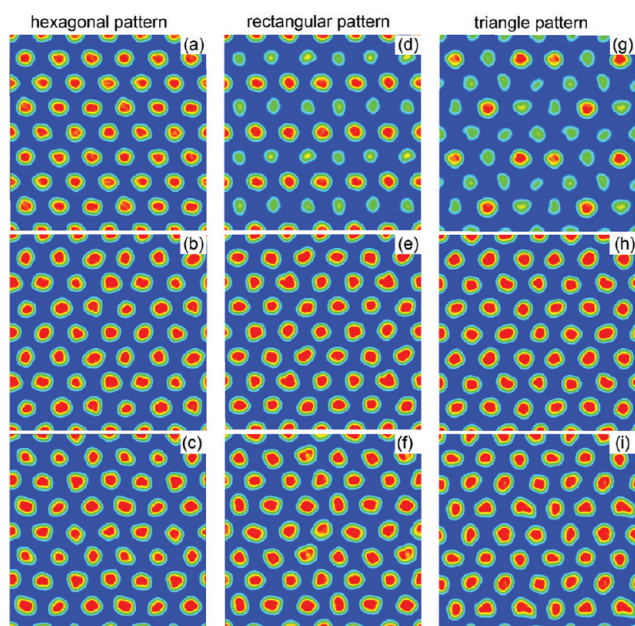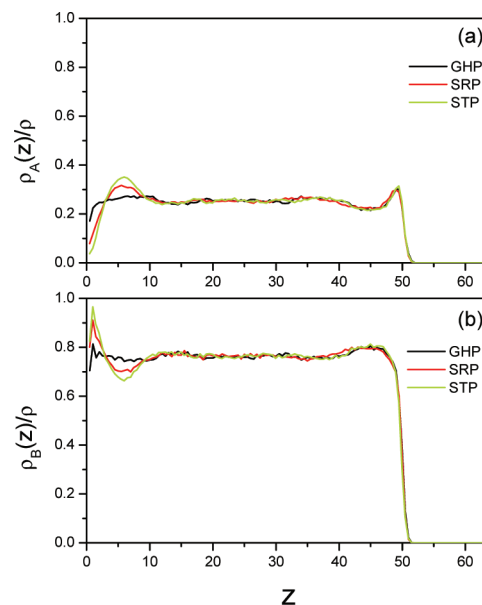
Figure 16. Cross sections of the bulk phase formed through template-guided self-assembly on the hexagonal pattern (left panels a, b, and c), sparse rectangular pattern (middle panels d, e, and f), and sparse triangle pattern (right panels g, h, and i), at different z: $z = 1$ (top panels a, d, and g), $z = 20$ (middle panels b, e, and h), and $z = 49$ (bottom panels c, f and i). Near the surface of the rectangular and triangle patterns, the detachment of A-rich domains from the substrate D-regions is evident, whereas slightly removed from the substrate, hexagonal morphology is seen. The regions rich in A and B components are shown in red and blue, respectively; intermediate regions are given in yellow and green. Note that all the cross sections are $2\times$ replicated.

Figure 17. Normalized density profiles for (a) A and (b) B beads of the copolymer melt in the direction perpendicular to the substrate for the films interacting with generic hexagonal pattern (GHP), sparse rectangular pattern (SRP), and sparse triangle pattern (STP).

replication to successively decrease with the increasing the film thickness.

Thus we can conclude that when the minority block-attractive substrate pattern period is commensurate with (or close to) the natural bulk periodicity, the vertical cylinders are registered almost perfectly with the surface pattern. In the absence of the guided pattern, however, the behavior can change dramatically. Typically, in this case the interior of the film has a mixed morphology (results not shown). This indicates clearly that the periodic surface pattern, which produces a periodic field with proper wavelength, is one of the key factors controlling the structure registration.

In general, our DPD simulations of template-guided BCP assembly predict qualitatively the same behavior as that observed in the SCFT calculations. What we would like, however, to emphasize here once again is that the quantitative agreement between the SCFT and DPD results is unlikely to be achieved in practice. In particular, the phase diagrams predicted by the two methods should be rather different, due to fluctuation effects, as one can expect, for example, from the comparisons made by Geisinger et al.,[64] who performed SCFT and Monte Carlo simulations for symmetric block copolymers confined into a thin film. Further, our DPD simulation results are consistent with those reported by Wang et al.,[77] who used Monte Carlo simulations on a simple cubic lattice to study the formation of cylindrical domains from compositionally asymmetric BCPs confined between a patterned substrate and an upper homogeneous wall. They observed long-range lateral ordering of perpendicular cylinders and their spatial fluctuations around equilibrium positions. A similar behavior can be seen in Figure 16.

For the sparse patterns (SRP and STP) considered here, the substrate-induced hexagonal arrangement of the minority domains in the xy plane is also observed in the DPD simulations. The vertical cylinders are registered and are epitaxial to the surface pattern (cf. Figures 15b,c and 16, middle and right panels).

We next looked in more detail on the mechanism of the pattern multiplication. In particular, as seen in Figures 15b,c and 16 (middle and right panels), the cross sections of the interpolated cylinders whose in-plane position does not coincide with the wettable regions on the pattern are noticeably deformed. In the vicinity of the substrate these domains are distorted from a nearly cylindrical shape to a cylindrical shape with end-caps, so that these cylinders practically do not contact the substrate. Nevertheless, in the interior of the film, there are no detectable differences in the density distribution for the hexagonal array of wettable spots and the two sparse patterns (cf. Figure 16, panels b, e, and h). The reconstruction of the bulk cylinder shape occurs for both sparse patterns at a distance from the patterned substrate approximately equal to the bulk cylinder diameter. At a distance from the substrate of 1.5 times the bulk cylinder diameter ($\sim 10\sigma$), the effect of the surface pattern is no longer apparent. Nearly the same behavior was observed in our SCFT calculations.

For the SRP, doubling the frequency of the pattern is observed for the resulting array of microdomains, while a 4-fold density multiplication is attained for the STP (Figure 15b,c). A similar template pattern interpolation has been found experimentally for a sparse hexagonal pattern.[37,42]

A more quantitative conclusion on the pattern-guided phase separation can be drawn from the density profiles $\rho_\alpha(z)$ in the direction perpendicular to the surface. They are displayed in Figure 17. The density profiles exhibit certain structure in the

25196

dx.doi.org/10.1021/jp204629k |*J. Phys. Chem. C* 2011, 115, 25185–25200

vicinity of the polymer/substrate interface: close to the polymer/substrate interface the film is enriched by the majority phase, followed by a layer which rich in the minority component. The structure in the density profiles fades away at around 10σ from the patterned surface so that the density of both components remains almost constant in the middle part of the film and is practically the same for all the patterns studied here. This is further evidence that the substrate-induced ordering is progressing into the bulk.

In the upper region of the simulation box occupied mainly by G particles, the density of polymer segments does not disappear completely (Figure 17). Although a zero density of polymer segments in this region is enthalpically favorable, a finite density observed for the polymer component implies that entropic contribution to the free energy of the system is significant at the "soft" polymer/gas interface.

4. CONCLUSIONS

Combining field-theoretic (SCFT) and particle-based (DPD) simulations, we have studied the template-directed self-assembly of cylinder-forming block copolymers in thin films deposited on patterned substrates with various distributions of alternating wettable and nonwettable regions. The effect of three types of patterned substrates — sparse hexagonal, rectangular and triangle patterns — has been examined. As simulation cells we used the boxes with two homogeneous and with homogeneous/heterogeneous binding surfaces (SCFT), as well as an asymmetric box with one hard wall and the other wall modeling a realistic "free surface" of a polymer film (DPD). Both SCFT and DPD simulations demonstrate that a stable hexagonal morphology with cylindrical microdomains arranged parallel to the substrate can be directed with remarkable precision into perpendicular phase by nanoscale substrate patterns. The surface control over the ordering and orientation of the hexagonal phase was regulated by the degree of commensurability between polymer and substrate patterning as well by the affinity between the minority domains and the pattern. For the sparse rectangular pattern with two different length scales and for the sparse hexagonal pattern we observed 2-fold and 4-fold multiplication, respectively, of the surface patterns density. A 2-fold resolution enhancement was also found for the sparse triangle pattern with two characteristic length scales. We emphasize that the approach discussed here allows the production of highly ordered equilibrium structures, i.e. the structures and their orientations which are robust to external perturbations.

The analysis of the circularly averaged structure factor allowed us to distinguish the structure orientation in a film. Additional peak in the region of small lateral wave numbers is attributed to undulational deformations of cylinder domains under preferable film boundaries. This theoretical work serves to rationalize modern nanolithographic fabrication of high-spatial-frequency arrays using lower-spatial-frequency templates.

◼ APPENDIX A: STRUCTURE FACTOR

The static structure factor $S(q)$ is an important characteristic describing the correlated density distribution in a molecular system.[57] This function allows one to identify the morphology of a microphase-separated block-copolymer system. The small-angle X-ray and neutron scattering experiments on a nanostructured material are based on the measurements of reflected wave's intensity. When radiation impinges on periodic structures with geometrical variations on the length scale of the wavelength of the radiation, measurable interference takes place if the number of periods is great enough to provide necessary signal-to-noise ratio.

Bulk period of order of tens nanometers characterizes typical periodic structures of block-copolymer melts. The same order of magnitude is usual for the thickness of thin BCP films. Therefore in the best case it is possible to observe only few periods of copolymer morphology along the normal to the substrate while the film may contain many periods along lateral directions. Consequently, measurable interference may be obtained from a big number of lateral periods.

We introduce the order parameter

$$\varphi(\mathbf{r}) = \varphi_A(\mathbf{r}) - f = 1 - f - \varphi_B(\mathbf{r}) \tag{A1}$$

characterizing the degree of microphase separation in a copolymer film. The structure factor is defined here as the Fourier transform of the order parameter $\varphi(\mathbf{r})$[57]

$$\Omega(\mathbf{q}) = \Omega(q_x, q_y, q_z)$$

$$= \left| \int_{sample} \varphi(\mathbf{r}) \exp(-i\mathbf{q}\mathbf{r}) \, \mathrm{d}^3\mathbf{r} \right|^2 \tag{A2}$$

where $\mathbf{q}$ is the wave vector. For thin BCP films, it is not convenient to analyze the structure factor in the form A2 which depends on three variables q_x, q_y, and $q_z \equiv q_\perp$. More suitable way is to use the circular average of $\Omega(q_x, q_y, q_z)$

$$S(q_\parallel, q_\perp) = \frac{1}{2\pi} \int_0^{2\pi} \Omega(q_\parallel \cos\varphi, q_\parallel \sin\varphi, q_\perp) \, \mathrm{d}\varphi \tag{A3}$$

where $q_\parallel = (q_x^2 + q_y^2)^{1/2}$ is the lateral component of $\mathbf{q}$. It should be stressed that the circular averaging of $\Omega(q_x, q_y, q_z)$ provides an increase in the signal-to-noise ratio and also decreases the number of independent components of $\mathbf{q}$ to be considered.

As mentioned above, the SCFT equations were solved pseudospectrally. This algorithm gives the Fourier expansion of the order parameter

$$\varphi(\mathbf{r}) = \sum_k \varphi_k \exp[i(q_{k,x}x + q_{k,y}y)] \cos(q_{k,z}z) \tag{A4}$$

where the wave vector $\mathbf{q}_k = (q_{k,x}, q_{k,y}, q_{k,z})$ takes discrete values from the set defined by the boundary conditions imposed on the rectangular box of dimensions $L_x = d$, $L_y = \sqrt{3}d$, $L_z = h$. Substituting the right-hand part of eq A4 into eq A2, we obtain a new representation for the static structure factor of a thin copolymer film

$$\Omega(\mathbf{q}) = \left| 2\pi^2 h \sum_k \varphi_k \delta(q_x - q_{k,x}) \delta(q_y - q_{k,y}) \right.$$

$$\times \left[\exp\left(-ih\frac{q_z + q_{k,z}}{2}\right) \mathrm{sinc}\left(h\frac{q_z + q_{k,z}}{2}\right) \right.$$

$$\left. \left. + \exp\left(-ih\frac{q_z - q_{k,z}}{2}\right) \mathrm{sinc}\left(h\frac{q_z - q_{k,z}}{2}\right) \right]\right|^2 \tag{A5}$$

where $\mathrm{sinc}(x) = \sin(x)/x$. The amplitudes φ_k and the corresponding harmonics $(q_{k,x}, q_{k,y}, q_{k,z})$ entering this expression are directly obtained in the course of SCFT calculations.

25197

dx.doi.org/10.1021/jp204629k |*J. Phys. Chem. C* 2011, 115, 25185–25200

The structure factor A5 is a continuous function of z; at the same time it is a discrete function of the lateral variables x and y. The RHS of eq A5 takes maximum values (with maximum of signal-to-noise ratio) when $|q_z|/q^* \ll 1$, where q^* is the length of wave vectors belonging to the set of the main harmonics. Typically, we set $0 \le |q_z|/q^* \le 0.1$ in our calculations.

■ APPENDIX B: DISSIPATIVE PARTICLE DYNAMICS FOR NPAT ENSEMBLE

One of the important aspects of the work presented here was to implement a Langevin NPAT barostat routine in DPD simulations for anisotropic box fluctuations. The NPAT (constant particle number, normal pressure, surface area, and temperature) ensemble is used to allow the dimensions of the system to adjust because the initial condition is not clearly known, or because volume fluctuations are of interest. In the general case, the equations of motion for the Langevin barostat are[71]

$$\dot{\mathbf{r}} = \mathbf{v} + \boldsymbol{\eta} \cdot \mathbf{r}$$
$$\dot{\mathbf{v}} = m^{-1}\mathbf{F} - \boldsymbol{\eta} \cdot \mathbf{v} - N_f^{-1} Tr[\boldsymbol{\eta}]\mathbf{v}$$
$$\boldsymbol{\eta} = M^{-1}[V(\mathbf{P} - \mathbf{P}_0) + N_f^{-1}(\sum_i m_i v_i^2)\mathbf{E} + \mathbf{R}] - \gamma_L \boldsymbol{\eta} \quad \text{(B1)}$$
$$\dot{\mathbf{H}} = \boldsymbol{\eta} \cdot \mathbf{H}$$
$$\dot{V} = Tr[\boldsymbol{\eta}]V$$

where $\mathbf{r}$, $\mathbf{v}$, and $\mathbf{F}$ ($= \mathbf{f}^{con} + \mathbf{f}^{dis} + \mathbf{f}^{ran}$) are the vectors of the positions, velocities, and forces, respectively; $N_f = 3(\mathcal{N}-1)$ is the number of degrees of freedom in the system ($\mathcal{N} = nN + n_G$); $\boldsymbol{\eta}$ is the tensor of the barostat friction coefficients and M and $\gamma_L = (3\mathcal{N}k_B T/4\pi^2 M)^{1/2}$ are their associated mass parameter and friction parameter, respectively; $\mathbf{E}$ is the unity matrix; $\mathbf{H}$ is the cell matrix whose columns are the three cell vectors $\mathbf{a}$, $\mathbf{b}$, and $\mathbf{c}$ (the system volume V is given by $V = \det(\mathbf{H})$); $\mathbf{P}_0$ is the external pressure tensor; and $\mathbf{P}$ is the instantaneous pressure tensor, which is given by the virial equation:

$$P_{\alpha\beta} = V^{-1}(\sum_i m_i(\mathbf{v}_i)_\alpha(\mathbf{v}_i)_\beta + \sum_i (\mathbf{f}_i^{con})_\alpha(\mathbf{r}_i)_\beta)$$
$$(\alpha, \beta = x, y, z) \quad \text{(B2)}$$

A stochastic (Langevin) tensor $\mathbf{R}$ entering eq B1 is drawn from Gaussian distribution with zero mean and unit variance scaled by $(2M\gamma_L k_B T/\Delta t)^{1/2}$ and defined as

$$\langle R_i(t)R_j(t')\rangle = 2M\gamma_L k_B T\delta_{ij}\delta(t - t') \quad \text{(B3)}$$

where Δt is the integration time step. The NPAT ensemble is introduce by semi-isotropic constraining of the barostat equation of motion shown in eq B4.

$$\frac{\mathrm{d}}{\mathrm{d}t}\eta_{\alpha\beta}(t) = \begin{cases} M^{-1}[V(t)(P_{zz}(t) - P_{zz}^{(0)}) + N_f^{-1}\sum_i m_i v_i^2(t) + R_{zz}(t)] - \gamma_L\eta_{zz}(t), & \alpha = \beta = z \\ 0, & \alpha, \beta \ne z \end{cases} \quad \text{(B4)}$$

In this model, the lateral box sizes L_x and L_y are fixed to maintain the constant surface area $A = L_x \times L_y$, whereas the height of the box L_z ($=h$) can fluctuate to adjust the internal normal pressure of the simulated system to the applied external pressure $P_{zz}^{(0)}$.

The equations of motion B1−B4 were integrated using a modified velocity Verlet scheme similar to that described by Jakobsen.[97] We used a time step $\Delta t = 0.05$ that ensures a proper integration of the equations of motion at $\gamma_L = 1$.

■ AUTHOR INFORMATION

Corresponding Author

*E-mail: khalatur@polly.phys.msu.ru (P.G.K); tsarkova@dwi.rwth-aachen.de (L.A.T).

■ ACKNOWLEDGMENT

■ REFERENCES

(1) Hamley, I. W. *The Physics of Block Copolymers*; Oxford University Press: New York, 1998; pp 432.

(2) *Block Copolymers in Nanoscience* Lazzari, M., Liu, G., Lecommandoux, S., Eds.; Wiley-VCH Verlag: Weinheim, Germany, 2006; p 447.

(3) Bates, F. S.; Fredrickson, G. H. *Phys. Today* **1999**, 52, 32–38.

(4) Hamley, I. W. *Nanotechnology* **2003**, 14, R39–R54.

(5) Matsen, M. W.; Schick, M. *Macromolecules* **1994**, 27, 6761–6767.

(6) Fredrickson, G. H. *The Equilibrium Theory of Inhomogeneous Polymers*; Oxford University Press: New York, 2006; p 437.

(7) Mansky, P.; Liu, Y.; Huang, E.; Russell, T. P.; Hawker, C. J. *Science* **1997**, 275, 1458–1460.

(8) Harrison, C.; Adamson, D. H.; Cheng, Z.; Sebastian, J. M.; Sethuraman, S.; Huse, D. A.; Register, R. A.; Chaikin, P. M. *Science* **2000**, 290, 1558–1560.

(9) Darling, S. B. *Prog. Polym. Sci.* **2007**, 32, 1152–1204.

(10) *Polymer Thin Films*; Tsui, O. K. C., Russell, T. P., Eds.; World Scientific: New York, 2008; p 312.

(11) Kim, H. C.; Park, S. M.; Hinsberg, W. D. *Chem. Rev.* **2010**, 110, 146–177.

(12) Tseng, Y.-Ch; Darling, S. B. *Polymers* **2010**, 2, 470–489.

(13) Fasolka, M. J.; Mayes, A. M. *Annu. Rev. Mater. Res.* **2001**, 31, 323–355.

(14) Cheng, J. Y.; Ross, C. A.; Chan, V. Z. H.; Thomas, E. L.; Lammertink, R. G. H.; Vancso, G. J. *Adv. Mater.* **2001**, 13, 1174–1178.

(15) Krausch, G.; Mergele, R. *Adv. Mater.* **2002**, 14, 1579–1583.

(16) Segalman, R. A. *Mat. Sci. Eng. R* **2005**, 48, 191–226.

(17) Stoykovich, M. P.; Nealey, P. F. *Mater. Today* **2006**, 9, 20–29.

(18) Black, C.; Guarini, K.; Breyta, G.; Colburn, M.; Ruiz, R.; Sandstrom, R.; Sikorski, E.; Zhang, Y. *J. Vac. Sci. Technol. B* **2006**, 24, 3188–3191.

(19) Black, C. T. *ACS Nano* **2007**, 1, 147–150.

(20) Hamley, I. W. *Prog. Polym. Sci.* **2009**, 34, 1161–1210.

(21) van Zoelen, W.; ten Brinke, G. *Soft Matter* **2009**, 5, 1568.

(22) Black, C.; Ruiz, R.; Breyta, G.; Cheng, J.; Colburn, M.; Guarini, K.; Kim, H. C.; Zhang, Y. *IBM J. Res. Dev.* **2010**, 51, 605–633.

(23) Tsarkova, L.; Sevink, G. J. A.; Krausch, G. *Adv. Polym. Sci.* **2010**, 227, 33–74.

25198

dx.doi.org/10.1021/jp204629k |*J. Phys. Chem. C* 2011, 115, 25185–25200

(24) Lin, Z.; Kim, D. H.; Wu, X.; Boosahda, L.; Stone, D.; LaRose, L.; Russell, T. P. *Adv. Mater.* **2002**, *14*, 1373–1376.

(25) Tsarkova, L.; Knoll, A.; Krausch, G.; Magerle, R. *Macromolecules* **2006**, *39*, 3608–3615.

(26) Park, M.; Harrison, C.; Chaikin, P. M.; Register, R. A.; Adamson, D. H. *Science* **1997**, *276*, 1401–1404.

(27) Rockford, L.; Liu, Y.; Mansky, P.; Russell, T. P.; Yoon, M.; Mochrie, S. G. *J. Phys. Rev. Lett.* **1999**, *82*, 2602–2605.

(28) Kim, S. O.; Solak, H. H.; Stoykovich, M. P.; Ferrier, N. J.; de Pablo, J. J.; Nealey, P. F. *Nature* **2003**, *424*, 411–414.

(29) Cheng, J. Y.; Mayes, A. M.; Ross, C. A. *Nat. Mater.* **2004**, *31*, 823–828.

(30) Stoykovich, M. P.; Muller, M.; Kim, S. O.; Solak, H. H.; Edwards, E. W.; de Pablo, J. J.; Nealey, P. F. *Science* **2005**, *308*, 1442–1446.

(31) Stoykovich, M. P.; Kang, H.; Daoulas, K. C.; Liu, G.; Liu, C. C.; de Pablo, J. J.; Müller, M.; Nealey, P. F. *ACS Nano* **2007**, *1*, 168–175.

(32) Segalman, R. A.; Schaefer, K. E.; Fredrickson, G. H.; Kramer, E. J.; Magonov, S. *Macromolecules* **2003**, *36*, 4498–4506.

(33) Edwards, E. W.; Montague, M. F.; Solak, H. H.; Hawker, C. J.; Nealey, P. F. *Adv. Mater.* **2004**, *16*, 1315–1319.

(34) Wang, J.-Y.; Chen, W.; Russell, T. P. Patterning with block copolymers. In *Unconventional Nanopatterning Techniques and Applications*; Rogers, J. A., Lee, H. H., Ed.; Wiley: Hoboken, NJ, 2009; pp 233−289.

(35) Saavedra, H. M.; Mullen, T. J.; Zhang, P.; Dewey, D. C.; Claridge, S. A.; Weiss, P. S. *Rep. Prog. Phys.* **2010**, *73*, 036501/1–036501/40.

(36) Cheng, J. Y.; Rettner, C. T.; Sanders, D. P.; Kim, H.-C.; Hinsberg, W. D. *Adv. Mater.* **2008**, *20*, 3155–3158.

(37) Ruiz, R.; Kang, H.; Detcheverry, F. A.; Dobisz, E.; Kercher, D. S.; Albrecht, T. R.; de Pablo, J. J.; Nealey, P. F. *Science* **2008**, *321*, 936–939.

(38) Bita, I.; Yang, J. K. W.; Jung, Y. S.; Ross, C. A.; Thomas, E. L.; Berggren, K. K. *Science* **2008**, *321*, 939–943.

(39) Tada, Y.; Akasaka, S.; Yoshida, H.; Hasegawa, H.; Dobisz, E.; Kercher, D.; Takenaka, M. *Macromolecules* **2008**, *41*, 9267–9276.

(40) Tada, Y.; Akasaka, S.; Takenaka, M.; Yoshida, H.; Ruiz, R.; Dobisz, E.; Hasegawa, H. *Polymer* **2009**, *50*, 4250–4256.

(41) Xiao, S.; Yang, X.; Park, S.; Weller, D.; Russell, T. P. *Adv. Mater.* **2009**, *21*, 2516–2519.

(42) Yang, X.-M.; Wan, L.; Xiao, S.; Xu, Y.; Weller, D. K. *ACS Nano* **2009**, *3*, 1844–1858.

(43) Ji, S.; Liu, C.-C.; Liu, G.; Nealey, P. F. *ACS Nano* **2010**, *4*, 599–609.

(44) Ji, S.; Nagpal, U.; Liao, W.; Liu, C.-Ch.; de Pablo, J. J.; Nealey, P. F. *Adv. Mater.* **2011**, *23*, 3692–3697.

(45) Park, S.; Lee, D. H.; Xu, J.; Kim, B.; Hong, S. W.; Jeong, U.; Xu, T.; Russell, T. P. *Science* **2009**, *323*, 1030–1033.

(46) Detcheverry, F. A.; Liu, G.; Nealey, P. F.; de Pablo, J. J. *Macromolecules* **2010**, *43*, 3446–3454.

(47) Detcheverry, F. A.; Pike, D. Q.; Nealey, P. F.; Müller, M.; de Pablo, J. J. *Faraday Discuss.* **2010**, *144*, 111–125.

(48) Liu, G.; Delcambre, S. P.; Stuen, K. O.; Craig, G. S. W.; de Pablo, J. J.; Nealey, P. F.; Nygård, K.; Satapathy, D. K.; Bunk, O.; Solak, H. H. *J. Vac. Sci. Technol. B* **2010**, *28*, C6B13–C6B19.

(49) Detcheverry, F. A.; Nealey, P. F.; de Pablo, J. J. *Macromolecules* **2010**, *43*, 6495–6504.

(50) Kang, H.; Detcheverry, F.; Stuen, K. O.; Craig, G. S. W.; de Pablo, J. J.; Gopalan, P.; Nealey, P. F. *J. Vac. Sci. Technol. B* **2010**, *28*, C6B24–C6B29.

(51) Nagpal, U.; Kang, H.; Craig, G. S. W.; Nealey, P. F.; de Pablo, J. J. *ACS Nano* **2011**, *5*, 5673–5682.

(52) Detcheverry, F. A.; Kang, H.; Daoulas, K. Ch.; Müller, M.; Nealey, P. F.; de Pablo, J. J. *Macromolecules* **2008**, *41*, 4989–5001.

(53) Detcheverry, F. A.; Pike, D. Q.; Nagpal, U.; Nealey, P. F.; de Pablo, J. J. *Soft Matter* **2009**, *5*, 4858–4865.

(54) Daoulas, K. C.; Müeller, M.; Stoykovich, M. P.; Kang, H.; de Pablo, J. J.; Nealey, P. F. *Langmuir* **2008**, *24*, 1284–1295.

(55) Detcheverry, F. A.; Kang, H.; Daoulas, K. C.; Müller, M.; Nealey, P. F.; de Pablo, J. J. *Macromolecules* **2008**, *41*, 4989–5001.

(56) Tang, Ch.; Lennon, E. M.; Fredrickson, G. H.; Kramer, E. J.; Hawker, C. J. *Science* **2008**, *322*, 429–432.

(57) Birkholz, M.; Fewster, P. F.; Genzel, C. *Thin Film Analysis by X-Ray Scattering*; Willey: Weinheim, Germany, 2006; p 378.

(58) Matsen, M. W. *Macromolecules* **2006**, *39*, 5512–5520.

(59) Drolet, F.; Fredrickson, G. H. *Phys. Rev. Lett.* **1999**, *83*, 4317–4320.

(60) Ceniceros, H. D.; Fredrickson, G. H. *Multiscale Model. Simul.* **2004**, *2*, 452–474.

(61) Kriksin, Yu. A.; Erukhimovich, I. Ya.; Khalatur, P. G.; Smirnova, Yu. G.; ten Brinke, G. *J. Chem. Phys.* **2008**, *128*, art. no. 244903.

(62) Kriksin, Yu. A., Erukhimovich, I. Ya., Smirnova, Yu. G., Khalatur, P. G., ten Brinke, G. *J. Chem. Phys.* **2009**, 130, art. no. 204901.

(63) Kriksin, Yu. A.; Khalatur, P. G.; Erukhimovich, I. Ya.; ten Brinke, G.; Khokhlov, A. R. *Soft Matter* **2009**, *5*, 2896–2904.

(64) Geisinger, T.; Müller, M.; Binder, K. *J. Chem. Phys.* **1999**, *111*, 5241–5250.

(65) Cavallo, A.; Müller, M.; Binder, K. *Macromolecules* **2006**, *39*, 9539–9550.

(66) Hoogerbrugge, P. J.; Koelmann, J. M. V. A. *Europhys. Lett.* **1992**, *19*, 155–160.

(67) Espanol, P.; Warren, P. B. *Europhys. Lett.* **1995**, *30*, 191–196.

(68) Groot, R. D.; Warren, P. B. *J. Chem. Phys.* **1997**, *107*, 4423–4335.

(69) Scocchi, G.; Posocco, P.; Fermeglia, M.; Pricl, S. *J. Phys. Chem. B* **2007**, *111*, 2143–2151.

(70) Groot, R. D.; Madden, T. G. *J. Chem. Phys.* **1998**, *108*, 8713–8724.

(71) Quigley, D.; Probert, M. *J. Chem. Phys.* **2004**, *120*, 11432–11441.

(72) Khokhlov, A. R.; Khalatur, P. G. *Chem. Phys. Lett.* **2008**, *461*, 58–63.

(73) Neratova, I. V.; Khalatur, P. G.; Khokhlov, A. R. *Chem. Phys. Lett.* **2010**, *487*, 297–302.

(74) Lyakhova, K. S.; Sevink, G. J. A.; Zvelindovsky, A. V.; Horvat, A.; Magerle, R. *J. Chem. Phys.* **2004**, *120*, 1127–1137.

(75) Horvat, A.; Lyakhova, K. S.; Sevink, G. J. A.; Zvelindovsky, A. V.; Magerle, R. *J. Chem. Phys.* **2004**, *120*, 1117–1126.

(76) Wang, Q.; Nealey, P. F.; de Pablo, J. J. *Macromolecules* **2001**, *34*, 3458–3470.

(77) Wang, Q.; Nealey, P. F.; de Pablo, J. J. *Macromolecules* **2003**, *36*, 1731–1740.

(78) Meng, D.; Wang, Q. *J. Chem. Phys.* **2007**, *126*, 234902–234911.

(79) Wang, Q. Monte Carlo simulations of nano-confined block copolymers. In *Nanostructured Soft Matter. Experiment, Theory, Simulation and Perspectives*; Zvelindovsky, A. V., Ed.; Springer: Dordrecht, The Netherlands, 2007; pp 495−527.

(80) Ji, S.; Liu, G.; Zheng, F.; Craig, G. S. W.; Himpsel, F. J.; Nealey, P. F. *Adv. Mater.* **2008**, *20*, 3054–3060.

(81) Han, E.; Stuen, K. O.; Leolukman, M.; Liu, C.-C.; Nealey, P. F.; Gopalan, P. *Macromolecules* **2009**, *42*, 4896–4901.

(82) Knoll, A.; Tsarkova, L.; Krausch, G. *Nano Lett.* **2007**, *7*, 843–846.

(83) Horvat, A.; Knoll, A.; Krausch, G.; Tsarkova, L.; Lyakhova, K. S.; Sevink, G. J. A.; Zvelindovsky, A. V.; Magerle, R. *Macromolecules* **2007**, *40*, 6930–6939.

(84) Matsen, M. W. *J. Chem. Phys.* **1997**, *108*, 7781–7791.

(85) Petera, D.; Muthukumar, M. *J. Chem. Phys.* **1998**, *109*, 5101–5107.

(86) Huinink, H. P.; Brokken-Zijp, J. C. M.; van Dijk, M. A. *J. Chem. Phys.* **2000**, *112*, 2452–2462.

(87) Chakraborty, A. K.; Golumbfskie, A. J. *Annu. Rev. Phys. Chem.* **2001**, *52*, 537–573.

(88) Chen, H.Yi.; Fredrickson, G. H. *J. Chem. Phys.* **2002**, *116*, 1137–1146.

(89) Alexander-Katz, A.; Moreira, A. G.; Fredrickson, G. H. *J. Chem. Phys.* **2003**, *118*, 9030–9036.

(90) Xu, T.; Zvelindovsky, A. V.; Sevink, G. J. A.; Lyakhova, K. S.; Jinnai, H.; Russell, T. P. *Macromolecules* **2005**, *38*, 10788–10798.

(91) Kim, S. O.; Kim, B. H.; Meng, D.; Shin, D. O.; Koo, C. M.; Solak, H. H.; Wang, Q. *Adv. Mater.* **2007**, *19*, 3271–3275.

(92) Bosse, A. W.; García-Cervera, C. J.; Fredrickson, G. H. *Macromolecules* **2007**, *40*, 9570–9581.

(93) Hur, S.-M.; García-Cervera, C. J.; Kramer, E. J.; Fredrickson, G. H. *Macromolecules* **2009**, *42*, 5861–5872.

(94) Edwards, E. W.; Montague, M. F.; Solak, H. H.; Hawker, C. J.; Nealey, P. F. *Adv. Matter* **2004**, *16*, 1315–1319.

(95) Ohta, T.; Ito, A. *Phys. Rev. E* **1995**, *52*, 5250–5260.

(96) Sigehuzi, T.; Tanaka, H. *Phys. Rev. E* **2004**, *70*, 051504/1–051504/8.

(97) Jakobsen, A. F. *J. Chem. Phys.* **2005**, *122*, 124901–124908.